Elemental composition of 433 Eros: New calibration of the NEAR-Shoemaker XRS data

Lucy F. Lim [a,*], Larry R. Nittler [b]

[a] Code 691, NASA/Goddard Space Flight Center, Greenbelt, MD 20771, USA
[b] Carnegie Institution of Washington, 5241 Broad Branch Road, NW, Washington, DC 20015, USA

ARTICLE INFO

ABSTRACT

We present a new calibration of the elemental-abundance data for Asteroid 433 Eros taken by the X-ray spectrometer (XRS) aboard the NEAR-Shoemaker spacecraft. (NEAR is an acronym for "Near-Earth Asteroid Rendezvous.") Quantification of the asteroid surface elemental abundance ratios depends critically on accurate knowledge of the incident solar X-ray spectrum, which was monitored simultaneously with asteroid observations. Previously published results suffered from incompletely characterized systematic uncertainties due to an imperfect ground calibration of the NEAR gas solar monitor. The solar monitor response function and associated uncertainties have now been characterized by cross-calibration of a large sample of NEAR solar monitor flight data against contemporary broadband solar X-ray data from the Earth-orbiting GOES-8 (Geostationary Operational Environmental Satellite). The results have been used to analyze XRS spectra acquired from Eros during eight major solar flares (including three that have not previously been reported). The end product of this analysis is a revised set of Eros surface elemental abundance ratios with new error estimates that more accurately reflect the remaining uncertainties in the solar flare spectra: Mg/Si = 0.753 + 0.078/−0.055, Al/Si = 0.069 ± 0.055, S/Si = 0.005 ± 0.008, Ca/Si = 0.060 + 0.023/−0.024, and Fe/Si = 1.678 + 0.338/−0.320. These revised abundance ratios are consistent within cited uncertainties with the results of Nittler et al. [Nittler, L.R., and 14 colleagues, 2001. Meteorit. Planet. Sci. 36, 1673–1695] and thus support the prior conclusions that 433 Eros has a major-element composition similar to ordinary chondrites with the exception of a strong depletion in sulfur, most likely caused by space weathering.

Published by Elsevier Inc.

1. Introduction

The Near Earth Asteroid Rendezvous (NEAR)-Shoemaker spacecraft orbited the Asteroid 433 Eros between February 2000 and February 2001. Among its mission objectives (Cheng, 1997) was the characterization of the surface composition of Eros using X-ray (XRS, Goldsten et al., 1997) and gamma-ray spectrometers (GRS, Goldsten et al., 1997). XRS results were published during and immediately after the mission by Trombka et al. (2000) and Nittler et al. (2001), but were plagued by systematic uncertainties stemming from the unlucky failure of one solar monitor and the incomplete pre-launch calibration of the other. This paper describes the subsequent effort at post-launch calibration of the NEAR gas solar monitor and the resulting improvement in our understanding of the XRS-derived elemental composition of 433 Eros.

The X-ray fluorescence emission measured by NEAR is a product of the interaction of solar X-rays with the asteroid's surface. As the asteroid is exposed to X-rays from the upper solar atmosphere, a fraction of the incident X-rays is photoelectrically absorbed by various inner electron shells of atoms in the surface, resulting in the emission of either an Auger electron or a fluorescent X-ray, with energies characteristic (Moseley, 1913) of the atoms that produce them.

Each electron shell can only be induced to fluoresce by that portion of the solar X-ray spectrum that falls above its binding energy. Moreover, fluorescent X-rays emitted by one atom may be absorbed by another atom in the asteroid's surface prior to escape into space. The resulting spectrum of fluorescent lines depends both on the abundance of each element in the asteroid's surface and on the spectral distribution of the incident X-rays. Accurate knowledge of the incident solar spectrum is thus critical to converting the spectra received by the NEAR XRS into elemental abundances on the asteroid's surface.

NEAR, therefore, carried two X-ray spectrometers dedicated to monitoring the solar spectrum between 1 and 10 keV. One of these, a Si PIN photodiode, failed prior to orbit insertion. The second consisted of a gas-filled proportional counter similar to the
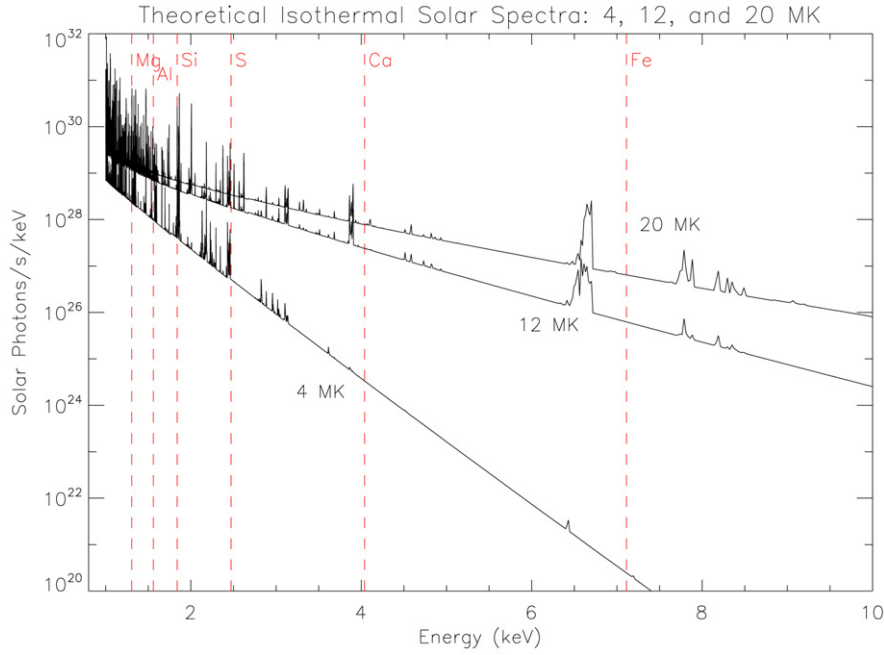
Fig. 1. Theoretical (CHIANTI 5.2; Dere et al., 1997; Landi et al., 2006) single-temperature solar spectra at three plasma temperatures. Vertical dashed lines represent the K edge energies of major elements measured by the NEAR XRS.

asteroid-pointing detectors, but covered by a graded filter (Clark et al., 1995) designed to attenuate the incoming solar flux and increase the dynamic range of the detector. Unfortunately, the response of this filter, particularly at off-normal solar incidence angles, was not adequately determined in the laboratory prior to launch.

This paper describes the post-launch calibration of the NEAR gas solar monitor and its application to the analysis of XRS spectra of 433 Eros acquired during eight major solar flares. The response of the graded filter and the uncertainties therein were modeled based on measurements and tolerances as recorded in the engineering diagrams. Resulting models of the gas solar monitor's response function were tested against flight data and checked against contemporaneous broadband X-ray data from the Earth-orbiting GOES-8 (Geostationary Operational Environmental Satellite) to reduce the range of possible solar monitor response functions to those that were consistent with the available data. Finally, the improved solar results were used to analyze data from eight major solar flares from which asteroid fluorescence was recorded by NEAR, resulting in a recalibrated elemental composition for 433 Eros. The remaining uncertainties in the solar spectra were incorporated into the error analysis for the asteroid's composition.

2. The solar X-ray spectrum

The solar X-ray output has been observed by instruments aboard a number of Earth-orbiting satellites. These have included various GOES (Geostationary Operation Environmental Satellites) broadband detectors; the SMM Bent Crystal Spectrometer (Acton et al., 1980) in the 1980s (1980, then 1984–1989); and the YOHKOH BCS and SXT (Bragg Crystal Spectrometer and Soft X-ray Telescope; Yoshimori et al., 1991) in the 1990s. After the NEAR mission, solar X-ray observations have also been conducted by the CORONAS-F X-ray spectrometer (RESIK; Sylwester et al., 2005) operated from 2001–2003, and RHESSI (Reuven Ramaty High-Energy Solar Spectroscopic Imager; Lin et al., 2002), launched in 2002.

The solar X-ray spectrum consists of a set of emission lines superimposed on a continuum. Emission lines in the region observed by NEAR (1–10 keV) come from highly ionized atoms (H and He–

like electron shells). The continuum is produced by bremsstrahlung emission, primarily from hydrogen, and declines steeply with increasing energy. Both the slope of the bremsstrahlung continuum and the intensities of the various emission lines vary greatly with electron temperature (Fig. 1). Electron temperatures (T_e) in the corona generally are in the range $\sim$2–30 $\times$ 10^6 K (e.g., Phillips, 2004), with the highest temperatures being reached only during major solar flares.

The amount of material at a given T_e is described by the "emission measure" (EM):

$$\text{EM} \equiv \int n^2 \, dV, \tag{1}$$

where n represents the plasma density and V is the volume of the hot plasma. The total spectrum for an isothermal plasma, then, is:

$$\phi_{\text{emitted}}(\lambda, T_e) = \left(E_{\text{ff}}(\lambda, T_e) + E_{\text{fb}}(\lambda, T_e) \right) \int n_e^2 \, dV \tag{2}$$

(Garcia, 1994), where E_{fb} is the emission line spectrum and E_{ff} is the bremsstrahlung continuum.

Generally, however, the solar spectrum is multithermal (e.g., Feldman et al., 1995; McTiernan et al., 1999). The thermal portion of the solar X-ray spectrum, then, can be represented by the integral over all temperatures of the amount of plasma at a given temperature (known as the "differential emission measure," DEM(T)) multiplied by the spectrum appropriate to that temperature:

$$\phi_{\text{total}}(\lambda) = \int \phi(\lambda, T) \times \text{DEM}(T) \, dT. \tag{3}$$

Typically, DEM(T) is calculated by observing the relative intensities of lines in the solar spectrum, since different species of ions have different emitting efficiencies as functions of temperature.

Because the NEAR gas solar monitor could not resolve individual spectral lines, its spectra do not contain enough information to permit full inversions of DEM(T). The typical structure of the DEM(T) of a solar flare represents two plasma components, one emitting at 5–10 MK and a hotter component emitting at 16–
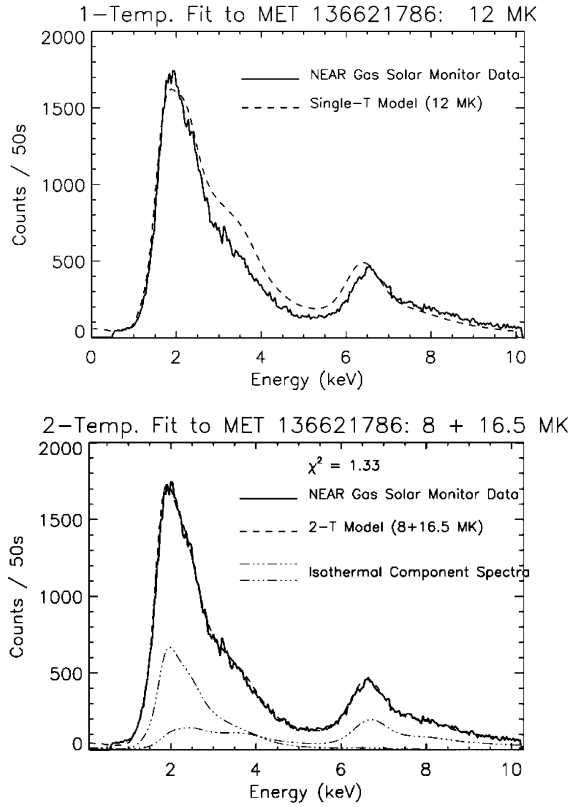
Fig. 2. Single-temperature (top) vs two-temperature fit to a NEAR solar monitor spectrum from 17-June-2000. The smooth dashed traces are the models, while the noisy solid ones are the NEAR data. In the lower plot, the dash-dotted traces are the two isothermal components of the fit. Two-temperature modeling was used throughout the present analysis.

25 MK (e.g., Antonucci and Dodero, 1995; Kepa et al., 2006).[1] We have therefore made the simplifying assumption that the solar X-ray spectrum can be adequately described by a two-temperature model, so that:

$$\phi_{total}(\lambda) = EM_1 \times \phi_1(\lambda, T_1) + EM_2 \times \phi_2(\lambda, T_2). \tag{4}$$

Fig. 2 illustrates single-temperature and two-temperature fits to a NEAR gas solar monitor flare spectrum.

2.1. Elemental abundances in the solar atmosphere

The line emission in the solar X-ray spectrum depends on the abundances of the emitting elements in the solar atmosphere as well as on the electron temperature. Generally, the X-ray emitting plasmas of solar flares reflect the composition of the solar corona, which differs substantially from that of the photosphere: in the corona, elements (other than hydrogen) with high first ionization potentials are depleted relative to elements with low first ionization potentials (the "FIP" effect). Although this relative fractionation according to FIP is well established, the absolute normalization of coronal abundances relative to photospheric ones is somewhat controversial (e.g., Fludra and Schmelz, 1999). In this work, we consider the published coronal abundances of Meyer (1985), based on observations in the extreme ultraviolet and X-ray ranges, and of Feldman et al. (1992).

Synthetic solar spectra were generated using the coronal abundances of both Meyer (1985) and Feldman et al. (1992) as inputs to

Table 1
Solar coronal abundances relative to hydrogen ($\log_{10}$ H = 12.0).

Element	$\log_{10}$ relative abundance				
	Meyer (1985)	Feldman et al. (1992)	Coronal 1	Coronal 2	Coronal 3
H	12.00	12.00	12.00	12.00	12.00
He	10.99	10.90	10.99	10.99	10.99
C	8.37	8.59	8.08	8.04	8.08
N	7.59	8.00	7.49	7.45	7.49
O	8.39	8.89	8.38	8.34	8.38
Ne	7.55	8.08	7.57	7.53	7.57
Na	6.44	6.93	6.42	6.38	6.42
Mg	7.57	8.15	7.64	7.60	7.64
Al	6.44	7.04	6.53	6.49	6.53
Si	7.59	8.10	7.59	7.55	7.59
S	6.94	7.27	6.76	6.72	6.76
Ar	6.33	6.58	6.07	6.03	6.07
Ca	6.47	6.93	6.42	6.38	6.42
Fe	7.59	8.10	7.59	7.55	7.29
Ni	6.33	6.84	6.33	6.29	6.33

the CHIANTI 5.2 code (Dere et al., 1997; Landi et al., 2006). In the latter calculation, a number of minor elements not included in the work of Feldman et al. (1992) were assigned abundances based on the photospheric abundances of Grevesse and Sauval (1998), with elements with low first-ionization potentials (FIP) increased by a factor of 3.5 for the "FIP" effect. These are the same values used in the "sun_coronal_ext" file included with the CHIANTI Solarsoft package (Landi et al., 2006).

Neither abundance set was entirely successful in modeling the NEAR gas solar monitor data: the spectra generated with the Feldman et al. abundances produced greatly superior matches in the region below 2.5 keV, but performed poorly above 6 keV; whereas the models using the Meyer abundances produced excellent fits to the data above 6 keV. Since the hydrogen-dominated bremsstrahlung continuum is an important contributor to the X-ray spectrum in the high-energy region where emission lines are relatively sparse, the overall metallicity of the Feldman et al. (1992) model was adjusted downward so that the Si/H ratio would be the same as that of Meyer (1985): Si/H = Fe/H = 3.9×10^{-5}. The resulting model produced a good fit to the NEAR data at all energies. Subsequently, additional models were tested with coronal metallicities varied to be slightly higher and slightly lower than those of the Meyer (1985) model. The two most successful models were those with Si/H = 3.5×10^{-5} ("Coronal 1" in Table 1) and Si/H = 3.9×10^{-5} ("Coronal 2"). Abundances in all relevant models are included in Table 1.

Flare-to-flare variation in solar elemental abundances has been observed by several investigators (Sylwester et al., 1984; Sterling et al., 1993; Fludra and Schmelz, 1999). For example, Sylwester et al. (1998) found that the calcium abundance varies from flare to flare over a factor of about 3.5 and is uncorrelated with electron temperature or GOES classification. Within a given flare and among flares associated with the same active region, however, the abundance was found to change only slowly. The NEAR gas solar monitor data from the major solar flare of 27 December 2000 (Section 6.5) proved impossible to fit with the same abundance sets that had worked for the other NEAR flare data. In particular, the 6.5 keV iron structure was clearly weaker with respect to the surrounding continuum than was the case in the spectra of other solar flares. For this reason, additional models were applied to this flare in which the abundance of iron was reduced by varying amounts.

3. The NEAR gas proportional counters

The energy resolution of the NEAR gas proportional counters, including the gas solar monitor and the three asteroid-pointing detectors, varied with energy according to FWHM = $0.340E^{1/2}$ (Starr

---

[1] The solar flares examined in these papers represented GOES classes C2–X2 and C8.1, respectively.
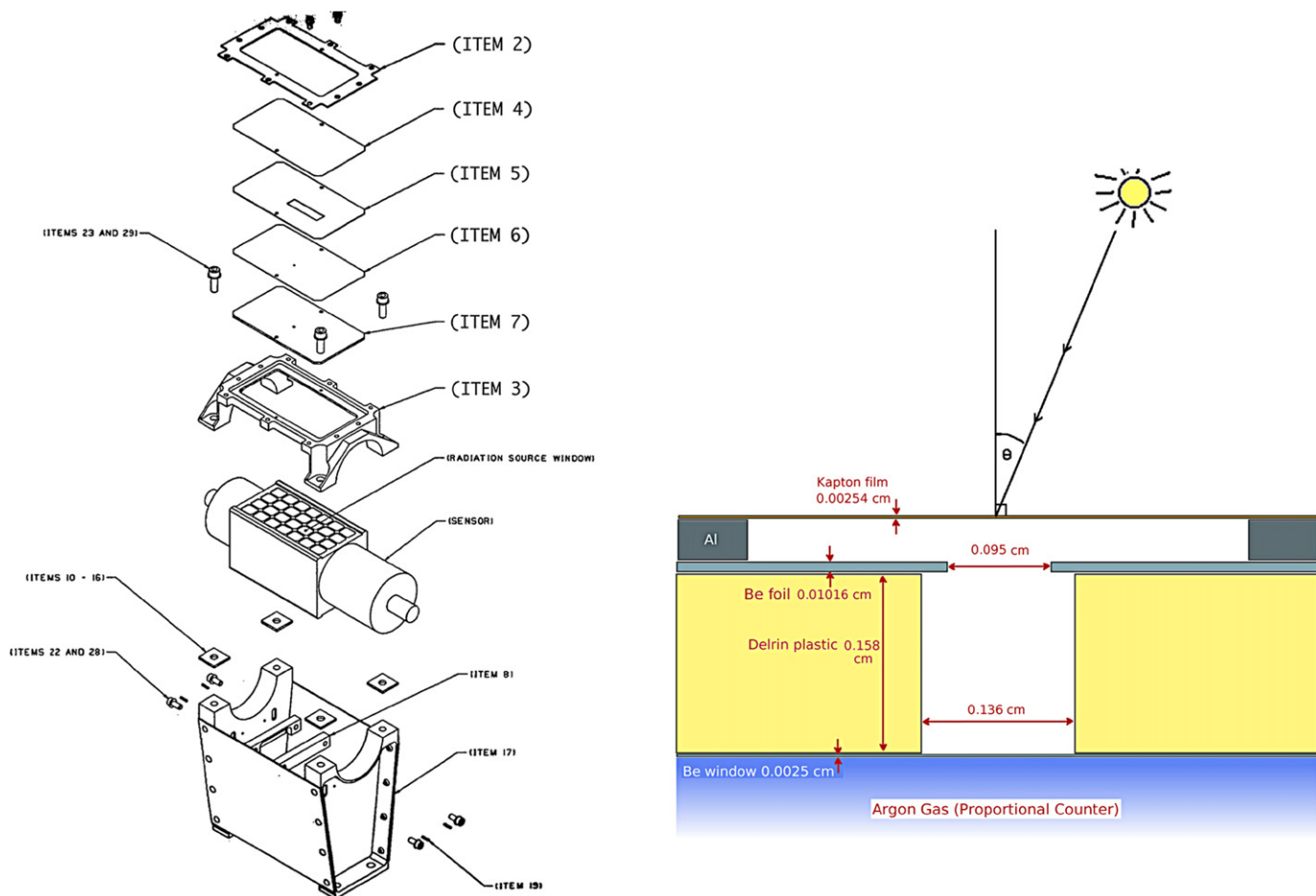
Fig. 3. Geometry of the NEAR gas solar monitor graded filter. Left: Engineering diagram of the graded filter assembly as mounted above the NEAR gas solar monitor tube. The filter pieces (Items 4–7) each measured 2×3.5 inches. Right: Schematic cross-section of the graded filter pinhole with nominal dimensions. The gas solar monitor was mounted on the sunward-facing deck of the NEAR-Shoemaker spacecraft so that the sensor face was parallel with the solar panels. Thus, the angle marked θ is the same as the "panel angle" of the spacecraft.

et al., 2000), where FWHM is the full width at half maximum of a Gaussian X-ray line. As discussed earlier, this resolution is not sufficient to resolve individual spectra lines in the solar X-ray spectrum, precluding inversion of the full DEM(T) (Eq. (3)) and limiting the information that can be obtained on solar elemental abundances. A potential drawback to our method of fitting solar monitor spectra to a two-temperature model (Fig. 2) is that the further the actual solar DEM(T) departs from the sum of two delta functions at two temperatures (for example, if there is a major mass of plasma contributing at a third temperature, or if the plasma temperature varies over a wide range such that a roughly equal amount of X-ray flux is contributed from each temperature increment ΔT), the poorer a representation of the actual solar spectrum our model will be.

Additional complications to modeling spectra from the NEAR gas detectors are due to escape peaks and pulse pile-up effects. The NEAR proportional counters were filled with P-10 (Starr et al., 2000), a standard mixture of 90% Ar and 10% CH$_4$. Methane does not significantly absorb X-rays in the 1–10 keV range; its purpose is to absorb the low-energy photons emitted by the argon in order to prevent spurious pulses. Argon, however, can cause an escape peak: if an incident X-ray induces fluorescence from an Ar atom and the fluorescent X-ray escapes the detector, the energy measured will be 2.97 keV (the K$_\alpha$ energy for Ar) below the original energy. Thus, an "escape peak" appears in the output spectrum for all incident energies higher than the binding energy of Ar (3.2 keV). For the NEAR detectors, the escape fraction was cal-

culated using Monte Carlo methods (R. Starr, 8 December 2004, personal communication), and was found to be well described by a linear function of energy.

At high count rates, such as those that occurred in the gas solar monitor during major solar flares, pulse addition in the detector electronics caused a pile-up effect in the entire spectrum, such that each channel would represent a higher energy than it did at low count rates. The size of this "zero shift" in the energy vs channel calibration increased with count rate, and was treated as a free parameter in the spectral fitting. For context, during the flares described in the present work, the overall calibration shifts ranged from $\approx$2–56 eV.

4. Modeling the NEAR gas solar monitor

The NEAR gas solar monitor was covered by a graded filter (Clark et al., 1995) intended to attenuate the incoming solar flux and increase the dynamic range of the detector (Fig. 3). Since the Sun's X-ray emission decreases steeply with increasing energy, the filter was designed to admit a greater proportion of "high-energy" ($\approx$4–9 keV) X-rays than low-energy ones.

The graded filter was constructed from thin layers of beryllium, aluminum, and the plastics Delrin and Kapton (Fig. 3). To prevent the proportional counter from being saturated, most of its area was covered by the Al layer. A broad slot (0.295 ± 0.005 by 1.181 ± 0.005 inches, or 2.25 cm^2) was cut out of the Al layer to admit a portion of the original incident solar radiation. The

Table 2
Nominal dimensions and engineering tolerances for the graded filter.

	Inches	Cm
Be pinhole diameter	0.0375 ± 0.0005	0.095 ± 0.00127
Delrin pinhole diameter	0.0535 ± 0.0005	0.136 ± 0.00127
Be thickness[a]	0.004 stock $+ 0.0006/$ -0.0001	$0.01016 + 0.0015/$ -0.0003
Delrin thickness[b]	0.062 stock	0.158
Kapton thickness[c]	0.001 stock ± 0.00015	0.0025 ± 0.00038
Al thickness[b]	0.015 stock	0.038
Be detector window thickness[d]		0.0025
Delrin density	1.425 g/cm^3	
Kapton density	1.42 g/cm^3	

[a] As measured by Goldsten (2003, personal communication). Tolerance not specified in engineering drawings.

[b] Not regarded as a critical dimension according to the engineering drawings; uncertainties unknown.

[c] According to Goldsten (2003), this "is the 100 HN process of Kapton by Dupont. The single point thickness is 0.85–1.15 mils for a 1.0 mil nominal thickness."

[d] Window of the off-the-shelf gas counter. Not part of the graded filter.

Delrin and Be layers underneath were pierced by concentric pinholes intended to allow a small fraction of the incident low-energy X-rays to reach the proportional counter underneath. Meanwhile, higher-energy X-rays would be relatively unimpeded by these materials.

The nominal dimensions of the pinholes and thicknesses of the graded filter layers are summarized in Table 2. These dimensions are critical for accurately determining the response of the gas solar monitor. Unfortunately, variations in these dimensions, even within the engineering tolerances of the filter, have substantial effects on the energy and angular response of the detector. The specified measurements come from the engineering drawings for the graded filter (Goldsten, 2003, personal communication). Given pinhole diameter uncertainties are the nominal engineering tolerances and material thicknesses are the specified stock thicknesses from the manufacturers.

Because the Delrin pinhole diameter was similar in dimension to the Delrin stock thickness (Fig. 3), the stock thickness is critically influential in determining the response function of filtered solar monitor at off-normal solar incidence angles. Unlike the pinhole diameters, however, the thicknesses of the filter layers were not marked as critical dimensions in the engineering diagrams. Regrettably, it has proven impossible to recover any pre-launch measurements that may have been made of these thicknesses. However, a leftover sample of the Be filter foil was later recovered by Goldsten et al. (1997) and measured after the fact to be on average 0.0042 inches thick, with individual measurements ranging from 0.0039 to 0.0046 inches. The Kapton stock was stated by the manufacturer (Richmond Aircraft Products) to be 1.0 mil (0.001 in.) in thickness, with single-point thicknesses ranging from 0.85 to 1.15 mils. No estimates of uncertainty were available on the thicknesses of the Delrin or aluminum stock or on the densities of the Delrin and Kapton plastics.

Attenuation coefficients for materials used in the proportional counter and graded filter were obtained from NIST (Hubbell, 1997, available at http://www.physics.nist.gov/PhysRefData/XrayMassCoef /cover.html).

4.1. Post-launch calibration of the filtered gas solar monitor

In order to reduce the uncertainties associated with the limitations of the pre-launch graded filter calibration, flight data from the NEAR mission were used to determine the range of plausible graded filter parameters consistent with the solar spectra collected during the mission. The parameter space within the engineering tolerances of the graded filter was searched systematically. Each

filter model was tested against actual gas solar monitor output at a wide range of incident angles and solar activity levels. One hundred sixty NEAR spectra were selected from solar flares that occurred between 4 May 2000 and 1 July 2000. Most of these flares occurred when the sunlit side of the asteroid was not in the field of view of the NEAR XRS, so are not represented in the asteroid-pointing data. For each NEAR spectrum, which represents a 50-s integration of the solar monitor, we generated a corresponding set of synthetic gas solar monitor spectra. Theoretical (CHIANTI 5.2: Dere et al., 1997; Landi et al., 2006) models of solar output at thirty-nine plasma temperatures between 2 and 40 MK were put through the response function of the candidate graded filter model, calculated at the correct solar incidence angle for the time of the observed spectrum, and then convolved with the response function of the gas counter. The best two-temperature fit according to a χ^2 test was then recorded, along with the temperatures and emission measures of the two isothermal components.

The free parameters in the fitting process were the temperatures of the two single-temperature spectra to be combined; the relative proportions of the low- and high-temperature components; the overall normalization, which is related to the emission measure of the spectrum; and the zero shift of the detector due to pile-up, as described in Section 3. Over a large sample of incidence angles and solar spectra, the lowest average χ^2 value should correspond to the graded-filter model that best described the flight hardware.

In addition to the goodness of the fit to the solar monitor output itself, the second test of our filter models was provided by contemporary data on solar X-ray emission provided by the GOES-8 satellite. Throughout June and August 2000, the asteroid–Sun–Earth angle was below 30°, so that during this period (but not, for example, during December 2000) GOES and NEAR were observing substantially the same portion of the Sun.

GOES-8 was equipped with two broadband X-ray channels: a short-wavelength channel with a bandpass of 0.5 to 4 Å (24.8 to 3.1 keV) and a long-wavelength channel at 1 to 8 Å (12.4 to 1.5 keV). Several investigators (Garcia, 1994; Feldman et al., 1995; Thomas et al., 1985) have published formulae for deriving temperatures from one or both of the GOES channel outputs. These were used by Trombka et al. (2000) in the earliest NEAR XRS paper to interpret the asteroid-pointing data, in place of the solar monitor; and similarly by Nittler et al. (2001) to interpret the "quiet sun" (non-flare) data. However, all of these GOES models are based on an isothermal approximation of the flare plasma. In order to test our new multithermal fits to the solar monitor data, we instead put each synthetic spectrum directly through the two GOES transfer functions (Thomas, 2003; Schwartz, 1998; Garcia, 1994) to model the outputs of the two channels. The ratio of the modeled channel outputs was then compared to the ratio of the actual GOES channel outputs ("GOES ratio") from the same time period, corrected for light time.

Based on the results of the χ^2 fitting and comparison to GOES data, eleven graded-filter models (Table 3) were selected for use in the asteroid-fluorescence data analysis. Eight of these represent the best χ^2 matches to the solar monitor data on the entire 160-spectrum test sample and the best matches to the GOES channel ratios in the subset (56 of the 160) taken from June 21 through July 1, when the Earth–Sun–asteroid angle was ⩽16.5°. With these eight models, the median χ^2 values for the 160 fits in the test sample were under 1.765 and median RMS matches of the calculated vs the measured GOES ratios under 0.032.

Three additional models were included. Model 9 was selected because it produced the lowest median χ^2 fit to the solar monitor data of any that was tested ($\chi^2 = 1.658$), although its performance on the GOES ratio test was slightly worse than that of a number of

Table 3
Selected graded filter models.

Model	Solar abundances	Filter parameters							Median χ^2	Median RMS GOES ratio
		Kapton thickness	Be pinhole	Delrin			Al thickness			
				Thickness	Pinhole	Density				
1	Coronal 1	+5%	−2%	−2%	+2%	Nom.	+5%		1.765	0.022
2	Coronal 1	+5%	Nom.	−2%	+2%	Nom.	+5%		1.761	0.027
3	Coronal 2	+5%	−2%	−6%	+3%	Nom.	+5%		1.744	0.026
4	Coronal 2	+5%	−2%	−4%	+2%	Nom.	+5%		1.716	0.024
5	Coronal 2	+5%	Nom.	−4%	+2%	Nom.	+15%		1.748	0.030
6	Coronal 2	+5%	Nom.	−4%	Nom.	Nom.	+5%		1.750	0.031
7	Coronal 2	+5%	−2%	−2%	−2%	−2%	+5%		1.722	0.029
8	Coronal 2	+5%	−1%	+2%	+2%	Nom.	+5%		1.714	0.024
9	Coronal 2	+5%	Nom.	Nom.	Nom.	Nom.	+15%		1.658	0.038
10	Coronal 1	−5%	Nom.	−4%	Nom.	Nom.	+10%		1.842	0.037
11	Coronal 1	+5%	Nom.	+2%	Nom.	Nom.	+10%		1.761	0.036

Table 4
Geometric information for eight solar flares.

Date	Flare MET range	Boresight latitude		Boresight longitude	
		First–last	Mean	First–last	Mean
4-May	MET 132826285-27185	+24.2–+7.9°	+16.8°	+139.4–+154.8°	+145.8°
20-May	MET 134210436-12886	+33.8–+38.5°	+36.7°	+151.5–+154.3°	+154.0°
15-Jun	MET 136508736-10886	+17.7––32.4°	−22.1°	+68.5––175.5°	+151.7°
17-Jun	MET 136620036-21786	−6.7––7.6°	−3.7°	+58.5–+169.3°	+63.8°
10-Jul	MET 138677136-80836	+2.5–+11.8°	+8.3°	−135.1––100.2°	−125.9°
27-Dec	MET 153341842-42742	−3.7–−7.4°	−4.9°	+163.3––174.9°	+174.3°
28-Dec	MET 153418442-19292	−23.8–−17.8°	−19.9°	−122.0––94.6°	−107.8°
2-Jan	MET 153832142-34142	−29.7––23.1°	−26.7°	+5.1–+144.0°	+110.0°

Date	Flare MET range	Incidence angle		Emission angle		Phase angle	
		First	Last	First	Last	First	Last
4-May	MET 132826285-27185	35.9°	20.7°	35.2°	58.8°	113.6°	113.7°
20-May	MET 134210436-12886	49.7°	30.5°	49.6°	47.2°	106.3°	104.3°
15-Jun	MET 136508736-10886	32.8°	77.0°	62.4°	47.5°	96.3°	94.9°
17-Jun	MET 136620036-21786	66.6°	43.7°	38.3°	39.6°	92.3°	100.2°
10-Jul	MET 138677136-80836	59.2°	55.4°	48.8°	40.3°	81.1°	87.8°
27-Dec	MET 153341842-42742	68.7°	43.5°	76.1°	42.2°	105.4°	105.5°
28-Dec	MET 153418442-19292	42.7°	85.3°	54.8°	27.4°	84.6°	86.4°
2-Jan	MET 153832142-34142	61.2°	64.2°	31.3°	35.7°	100.4°	101.9°

Date	Flare MET range	Solar monitor (panel) angle	
		Range	Mean
4-May	MET 132826285-27185	35.2–35.7°	35.5°
20-May	MET 134210436-12886	14.9–19.5°	17.3°
15-Jun	MET 136508736-10886	22.7–23.6°	23.2°
17-Jun	MET 136620036-21786	20.3–25.5°	21.7°
10-Jul	MET 138677136-80836	3.2–10.1°	7.8°
27-Dec	MET 153341842-42742	16.0–17.5°	16.7°
28-Dec	MET 153418442-19292	29.7–29.7°	29.7°
2-Jan	MET 153832142-34142	20.3–23.8°	22.1°

other models. (Model 1, which produced the lowest median RMS to the GOES channel ratios—0.022—was already included among the first eight models.) Models 10 and 11 represented "local minima" in both χ^2 and GOES ratio RMS comparisons; 10 was the only model that performed well in which the Kapton layer was as thin or thinner than its nominal stock thickness, and 11 was the best-performing model among those in which the Delrin was as thick or thicker than its nominal stock thickness. Although the eight overall best models all had thick Kapton and thin Delrin layers, the performance of these two models was close enough that they could not be ruled out on the basis of the available data.

5. Application of the solar monitor results to the determination of asteroid elemental abundance ratios

We have applied the new solar monitor models in a new analysis of asteroid XRS spectra for eight solar flares: five from May–July 2000, two from December 2000, and one from 2 January 2001. Note that these include the five flares analyzed by Nittler et al. (2001) and three additional flares for which data have not previously been reported. The time and geometric information for the analyzed flares are provided in Table 4.

The procedure used to determine surface abundance ratios of Eros from NEAR XRS data acquired during solar flares followed closely that used by Nittler et al. (2001). The steps to this pro-
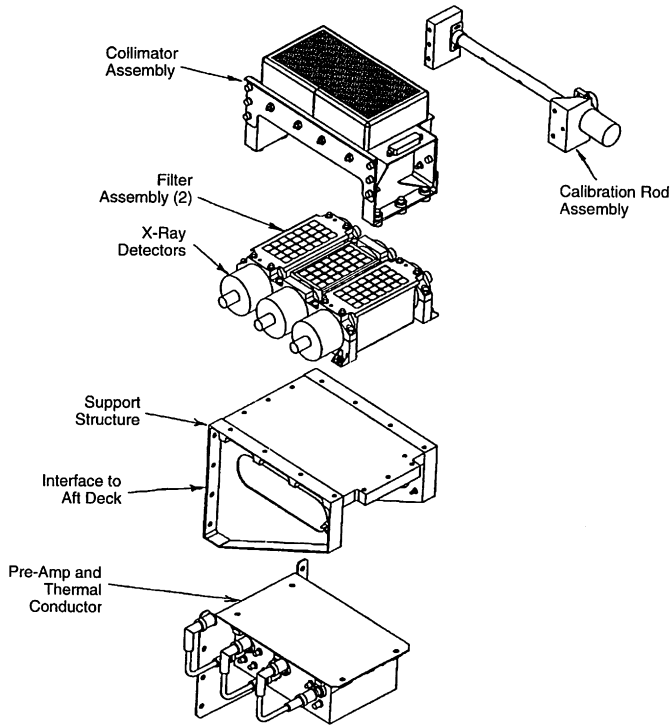
Fig. 4. Assembly of the NEAR X-ray asteroid-pointing sensors (Fig. 7 from Goldsten et al. (1997), reprinted by kind permission of Springer Science and Business Media). To enable analysis of the low-energy X-ray lines, one detector was filtered with a thin layer of Al and another was similarly equipped with a Mg filter. The center detector remained unfiltered. The rectangular faces of the gas counter tubes ("X-ray detectors") were each 2×3.5 inches, as with the gas solar monitor tube (Fig. 3). The same model tubes were used in both cases.

cess were: determination of the appropriate solar X-ray spectrum from solar monitor data, extraction of the photon flux in each of the major fluorescent lines from the asteroid-pointing spectra, generation of calibration curves relating photon ratios to abundance ratios for a specific incident solar spectrum and viewing geometry, and conversion of photon flux ratios to abundance ratios.

Solar models for each flare were produced using all eleven graded filter models, selected as described above. For each filter model, each 50-s integration of the gas solar monitor was fit with a two-temperature model of the solar spectrum, resulting in a model solar spectrum with sufficient energy resolution to distinguish individual solar emission lines. The 50-s two-component model spectra were then co-added to produce a time-integrated solar flare spectrum representing the same time interval as the co-added asteroid spectra (Section 5.2).

The fitting process used to extract asteroid fluorescence counts from the asteroid-pointing detector spectra is identical to that described in Nittler et al. (2001), with the exception that the on-board energy calibration data has now been analyzed and applied to constrain the properties of the proportional counters, as described below.

5.1. Calibration of the asteroid-pointing detectors with the on-board ^{55}Fe sources

Nittler et al. (2001) allowed the gains and zeroes of the three asteroid-pointing detectors to float as free parameters in their previous analysis of data from five NEAR solar flares. However, the NEAR XRS included three radioactive ^{55}Fe calibration sources ("Calibration Rod Assembly" in Fig. 4) to monitor the gain (eV/channel), zero (energy of channel zero), and energy resolution of the asteroid-pointing detectors. Several times throughout

Table 5

XRS asteroid-pointing detector calibration data fitting results. Detector resolution is a function of energy: $\text{FWHM}(E) = \text{FWHM parameter} \times E^{1/2}$.

Date	Gain	Zero	FWHM parameter
	Al-filtered		
26-Apr-2000	0.0386 ± 0.0002	-0.01 ± 0.04	0.385 ± 0.003
10-May-2000	0.0382 ± 0.0003	$+0.02 \pm 0.04$	0.375 ± 0.004
24-May-2000	0.0381 ± 0.0003	$+0.02 \pm 0.04$	0.367 ± 0.004
7-Jun-2000	0.0391 ± 0.0003	-0.09 ± 0.05	0.409 ± 0.004
8-Jun-2000	0.0384 ± 0.0003	$+0.03 \pm 0.03$	0.391 ± 0.005
12-Dec-2000	0.0378 ± 0.0002	$+0.03 \pm 0.04$	0.367 ± 0.004
09-Jan-2001	0.0381 ± 0.0002	-0.05 ± 0.04	0.364 ± 0.004
	Mg-filtered		
25-Apr-2000	0.0397 ± 0.0001	$+0.02 \pm 0.02$	0.361 ± 0.002
3-May-2000	0.0397 ± 0.0002	$+0.00 \pm 0.03$	0.358 ± 0.003
16-May-2000	0.0392 ± 0.0002	$+0.05 \pm 0.02$	0.344 ± 0.002
23-May-2000	0.0395 ± 0.0001	$+0.01 \pm 0.02$	0.349 ± 0.002
30-May-2000	0.0407 ± 0.0003	$+0.00 \pm 0.01$	0.428 ± 0.004
6-Jun-2000	0.0399 ± 0.0002	$+0.03 \pm 0.03$	0.378 ± 0.003
2-Jan-2001	0.0402 ± 0.0002	$+0.02 \pm 0.02$	0.373 ± 0.002
	Unfiltered		
27-Apr-2000	0.037 ± 0.002	$+0.2 \pm 0.3$	0.33 ± 0.02
11-May-2000	0.035 ± 0.004	$+0.4 \pm 0.7$	0.30 ± 0.05
25-May-2000	0.038 ± 0.003	$+0.0 \pm 0.4$	0.37 ± 0.04
20-Dec-2000	0.037 ± 0.002	$+0.3 \pm 0.3$	0.37 ± 0.03

Table 6

Unfiltered detector characteristics derived from flare data.

Date	Gain	Zero	FWHM
4-May-2000	0.0386 ± 0.0002	-0.06 ± 0.01	0.365 ± 0.007
20-May-2000	0.0378 ± 0.0008	-0.03 ± 0.03	0.366 ± 0.013
2-Jun-2000	0.0395 ± 0.0020	-0.10 ± 0.11	0.430 ± 0.065
15-Jun-2000	0.0387 ± 0.0006	-0.05 ± 0.03	0.371 ± 0.016
17-Jun-2000	0.0384 ± 0.0007	-0.03 ± 0.03	0.380 ± 0.018
10-Jul-2000	0.0375 ± 0.0007	-0.02 ± 0.03	0.350 ± 0.013
27-Dec-2000	0.0389 ± 0.0003	-0.05 ± 0.01	0.375 ± 0.012
28-Dec-2000	0.0391 ± 0.0006	-0.07 ± 0.03	0.351 ± 0.010
1-Jan-2001	0.0387 ± 0.0005	-0.06 ± 0.02	0.354 ± 0.011

the mission (Table 5) the calibration sources were rotated into the fields of view of their respective detectors for the acquisition of calibration data. Making use of the in-flight calibration data reduces the number of free parameters, increasing confidence in the fitting results. This is especially important for the two filtered detectors, in which count rates from the asteroid were always low in comparison with the cosmic-ray-induced background.

The ^{55}Fe sources emitted X-rays in the Mn K_α (88%) and K_β (12%) lines at 5.898 and 6.490 keV, respectively. The detectors also registered escape peaks for the two lines at 2.941 and 3.533 keV. For every available set of calibration data, the detectors' response to the pair of monoenergetic lines received from the ^{55}Fe source was modeled and fit to the calibration data. Gaussian shapes were assumed for all four peaks. The scale of the cosmic-ray background, whose shape was established by calibration-source- and asteroid-free data taken within 24 h of the calibration data, was also allowed to float, but usually remained within 1% (and always within 2%, for the two filtered detectors) of simple scaling by integration time. Calibration source fitting results are summarized in Table 5.

The ^{55}Fe source for the unfiltered detector was much weaker than the sources for the other two detectors, resulting in poor statistics on its calibration data and consequently relatively large error bars on its gain, zero, and FWHM parameters in Table 5. However, the unfiltered detector had the best statistics of the three in the asteroid fluorescence during the solar flares themselves, and more precise detector characteristics could be derived from the flare spectra themselves (Table 6). In contrast, the calibration
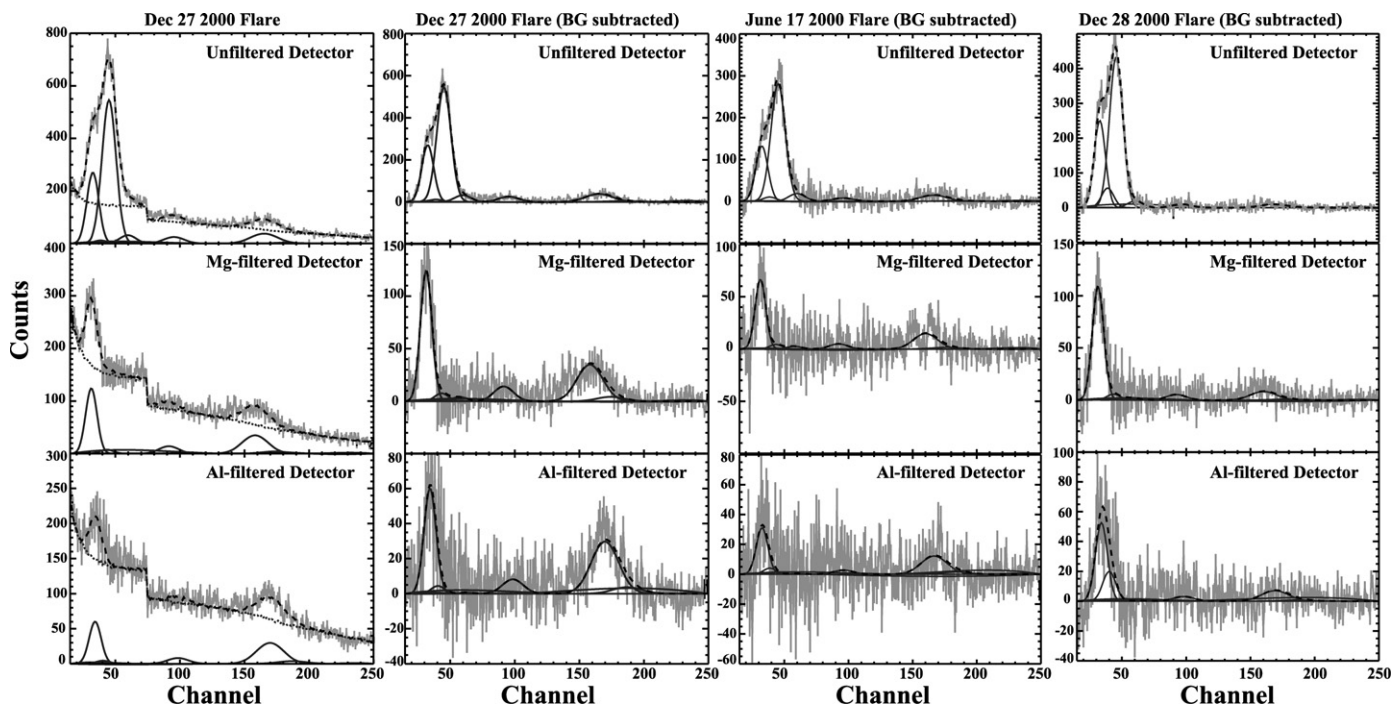
Fig. 5. XRS data from the three asteroid-pointing detectors. Left to right: Raw data from the solar flare of 27-Dec-2000; background-subtracted data from 27-Dec-2000; background-subtracted data from the flare of 17-Jun-2000; background-subtracted data from the flare of 28-Dec-2000. The step at channel 75 in the raw data is the rise-time discriminator limit. Solid lines represent the best Gaussian fits to individual XRF peaks; dashed traces represent the sum of all components. From left to right, the peaks are Mg, Al, Si, S, Ca, and Fe (K_α and K_β).

source data gave better statistics than the flare data for the two filtered detectors.

The energy resolution was the most variable of the detector characteristics, becoming degraded whenever the instrument was shut off, for example when the spacecraft was placed in safe mode, and taking several weeks to approach its best value (FWHM parameter = 0.340). This can be observed in Table 5, as the resolutions of the Al and Mg detectors improve slowly from April to late May.

5.2. Extracting photon counts from the asteroid-pointing detector data

As with the solar monitor data, the spectra from the asteroid-pointing detectors were recorded in 50-s integrations. For each solar flare, all the spectral integrations from that flare were co-added to generate a single summed flare spectrum for each asteroid-pointing detector. Cosmic-ray induced background, present in all of the gas proportional counters, was then subtracted from each co-added spectrum prior to fitting. Since this background was constant on time scales of a few hours, background spectra were derived for each detector from data taken within 24 h of the flare while the asteroid was not in the XRS field of view. These "dark" spectra were added together and scaled to the live time of the relevant flare spectra. Examples of co-added asteroid spectra before and after background subtraction are plotted for the 27 December 2000 flare in Fig. 5.

Following background removal, the spectra from the three detectors were fit simultaneously, allowing the Mg- and Al-filters to perform their design function: to compensate for the low resolution of the proportional counters at the K_α energies of the light elements Mg, Al, and Si. The free parameters in the spectral fitting were the intensities of the fluorescence lines from each major element (Mg, Al, Si, S, Ca, and Fe) entering the top of the instrument, as well as the gains, zeroes and FWHM parameters of the detectors. For the unfiltered detector, the detector parameters were allowed to vary freely; while for the Mg- and Al-filtered detec-

tors, they were allowed to float within the limits derived from the calibration-source data (Table 5) closest to the date of the flare.

The fitting process for three solar flares is illustrated in Fig. 5. In each plot, the grey lines with error bars represent the data from each asteroid-pointing detector. Error bars are 1σ, reflecting counting statistics. The leftmost plot shows the raw asteroid-pointing data from the flare of 27 December 2000, whereas the three remaining plots show the data after the cosmic-ray background has been subtracted. The fit to each of the individual fluorescence lines is represented by a solid Gaussian trace. From lowest- to highest-energy, these are the K_α lines of Mg, Al, Si, S, Ca, and Fe and the K_β line of Fe. The effect of the balanced-filter system can easily be observed in these plots: the Si line, which is the most prominent feature in the unfiltered data (top plots), has been suppressed in the data from the two filtered detectors. The superimposed dashed trace is the overall fit to the data. Similar plots representing the five previously analyzed flares were printed in Nittler et al. (2001).

5.3. Conversion of photon ratios to asteroid elemental ratios

The amount of fluorescence in any line that escapes the asteroid depends not only on the abundance of the fluorescing element, but also on the abundance of all other elements in the asteroid surface that can absorb incident solar radiation on the way in or fluorescent radiation on the way out. Because of this, it is necessary to make some assumptions about the entire composition of the asteroid in order to interpret the XRS data, including elements whose fluorescence could not be detected. We based our determination of the relationships between fluorescence ratios and elemental ratios on data from meteorites.

Once the incident solar spectrum was modeled, theoretical X-ray spectra (including both fluorescence and coherent scattering components) that would be induced by the model solar spectrum at the applicable incidence, emission, and phase angles were cal-

Table 7

Meteorite samples used to convert photon ratios to element ratios.

Meteorite	Ref. num.[a]	Class
ALH77081	1	Acapulcoite
Bustee	2	Aubrite
Brachina	3	Brachinite
Bali	3	CV3
A881526	4	Diogenite
Y793164	4	Monomict Eucrite
Brient	5	Polymict Eucrite
Y790113	4	Polymict Eucrite
Avanhandava	3	H4
Ipiranga	3	H5
Pulsora	3	H5
El Taco	3	IAB
Semarkona	3	LL3
Greenwell Spr.	3	LL4
Cherokee Spr.	3	LL6
Y74357	4	Lodranite
Y791493	4	Lodranite
Ilimaes	6	Pallasite
Jalanash	4	Ureilite
Y074659	4	Ureilite
ALH77257	3	Ureilite
Semarkona	3	LL3[b]

[a] References: (1) Nagahara and Ozawa (1986), (2) Watters and Prinz (1979), (3) Jarosewich (1990), (4) Yanai and Kojima (1995) (book), (5) Dyakonova and Kharitonova (1961) (Russian), (6) Buseck (1977). All analyses are whole-rock except for the El Taco silicate inclusion in a IA iron.

[b] Used by Nittler et al. (2001) as the basis for an "LL3 without sulfur" composition. The sulfur abundance was set to zero and all other elements normalized to 100%.

culated for a sample of meteorite compositions of widely different classes (Table 7). This is the same method described and used by Nittler et al. (2001). The model X-ray spectra for the different meteorite compositions were then fit using exactly the same method as had been applied to the actual XRS spectra to derive model fluorescence ratios. Calibration curves were calculated by plotting actual meteorite elemental abundance ratios against modeled meteorite fluorescence ratios and fitting quadratic curves to these points. Each quadratic fit provided the formula for converting fluorescent–photon ratios to elemental ratios for a particular incident solar spectrum and geometry. Fig. 6 illustrates the calibration curves for the solar spectrum and geometry of the major flare from 17 June 2000.

As in Nittler et al. (2001), the coherent scattering background has been accounted for by inclusion in these calculated meteorite fluorescence ratios rather than by any attempt to subtract it from the fluorescent photon signal. The induced Al fluorescence from the Al filter in front of the Al-filtered detector has been treated similarly. Because the theoretical spectra are treated exactly the same way as the real data, this does not introduce significant errors. However, because the derived fluorescence counts include scattered photons and filter fluorescence, the photon ratios for Al/Si and S/Si in the calibration curves (Fig. 6) are nonzero even at zero concentrations of Al and S.

The angles used in these calculations were averages over those provided in the XRS data products for the individual spectral integrations during a flare. The phase angles were exact, but the incidence and emission angles were averages over all the "plates" of the shape model derived from the NEAR laser rangefinder data (Zuber et al., 2000) that were illuminated and within the XRS field of view at the time. These derived angles varied much more during flares than did the phase angles (Table 4) and thus, in principle, calibration curves should be determined for each integration. However, the statistics did not permit separate fitting of integrations over small time portions within a single flare. Modeling of expected X-ray spectra for an ordinary chondrite composition illu-

minated by a typical solar flare at a fixed phase angle, but with varying incidence and emission angles, indicated that the uncertainty introduced by using averaged incidence and emission angles is significantly smaller than that caused by other sources of error in our analysis, for example the solar modeling. Moreover, the incidence and emission angles that matter physically for X-ray interactions are on a much smaller scale than any possible shape model of the asteroid, so this issue is a fundamental limitation in the analysis of NEAR XRS data.

In their XRS analysis, Nittler et al. (2001) applied an additional correction to the data to take into account the fact that in meteorites (and hence probably stony asteroids), the elements are not spread uniformly throughout the asteroidal material, but rather tend to be segregated into different minerals on spatial scales that are important to X-ray absorption and scattering. Nittler et al. (2001) derived "mineral mixing corrections" based on comparisons of theoretical spectra for mixtures of the dominant individual minerals found in anhydrous meteorites (olivine, pyroxene, feldspar, Fe–Ni metal and iron sulfide) with those for homogeneous mixtures of the same bulk compositions. The average correction factors (from Table 2 in Nittler et al., 2001) are reprinted here in Table 9. If applied, the largest effects are to increase the S/Si and Fe/Si ratios by 30–40% and decrease Al/Si by 25%. We note that the magnitude of the Fe/Si correction factor depends strongly on the amount of metallic Fe present in the material.

Recently, Foley et al. (2006) have questioned the necessity of the mineral-mixing correction for NEAR XRS data on the grounds that impact processing is likely to have reduced Eros' regolith to a well-mixed homogeneous powder. Moreover, calibration data for the Mars Pathfinder alpha-proton X-ray spectrometer (APXS) for powdered samples (with grain sizes of tens of microns) of meteorites with a large variation in metal abundances gave correct compositions without requiring such a correction (Foley, 2002). Additional experiments are needed to clarify whether mineral-mixing corrections are required and we therefore report both corrected and uncorrected versions of the asteroid composition (Table 9).

6. Fitting results for specific solar flares

The fitting results for the eight solar flares are summarized in Table 8 and discussed below. Results for five of these (4-May-2000, 15 June, 10 July, 27 December, and 2-January-2001) are revisions of those previously presented by Nittler et al. (2001). For these, the new photon ratios remain generally consistent with published results (Nittler et al., 2001, Table 3). Three additional flares for which data have not previously been reported (20 May, 17 June, 28 December) are also presented here.

Note that for many of the flare data, derived Al photon counts and Al/Si photon ratios were very sensitive to any limits placed on the zero point of the Al-filtered detector. For example, for the 4-May-2000 flare, calibration-source data from April 26 and May 10 (Table 5) suggest that the Al detector zero should be above -0.04. When so limited, the Al/Si photon ratio is 0.092 ± 0.032. However, if the Al-filtered detector zero is allowed to float without a limit, its value drops to -0.09 and the Al/Si photon ratio to 0.066 ± 0.024. The discrepancy between these solutions has been treated as a systematic uncertainty and is included in the total uncertainty quoted for this and other flares in Table 8. The effects on the other element ratios were minor compared to the uncertainties from counting statistics.

6.1. 4 May 2000

The May 4, 2000 solar flare induced more asteroid fluorescence from the high-Z elements (Fe, Ca, and S) than any other solar flare
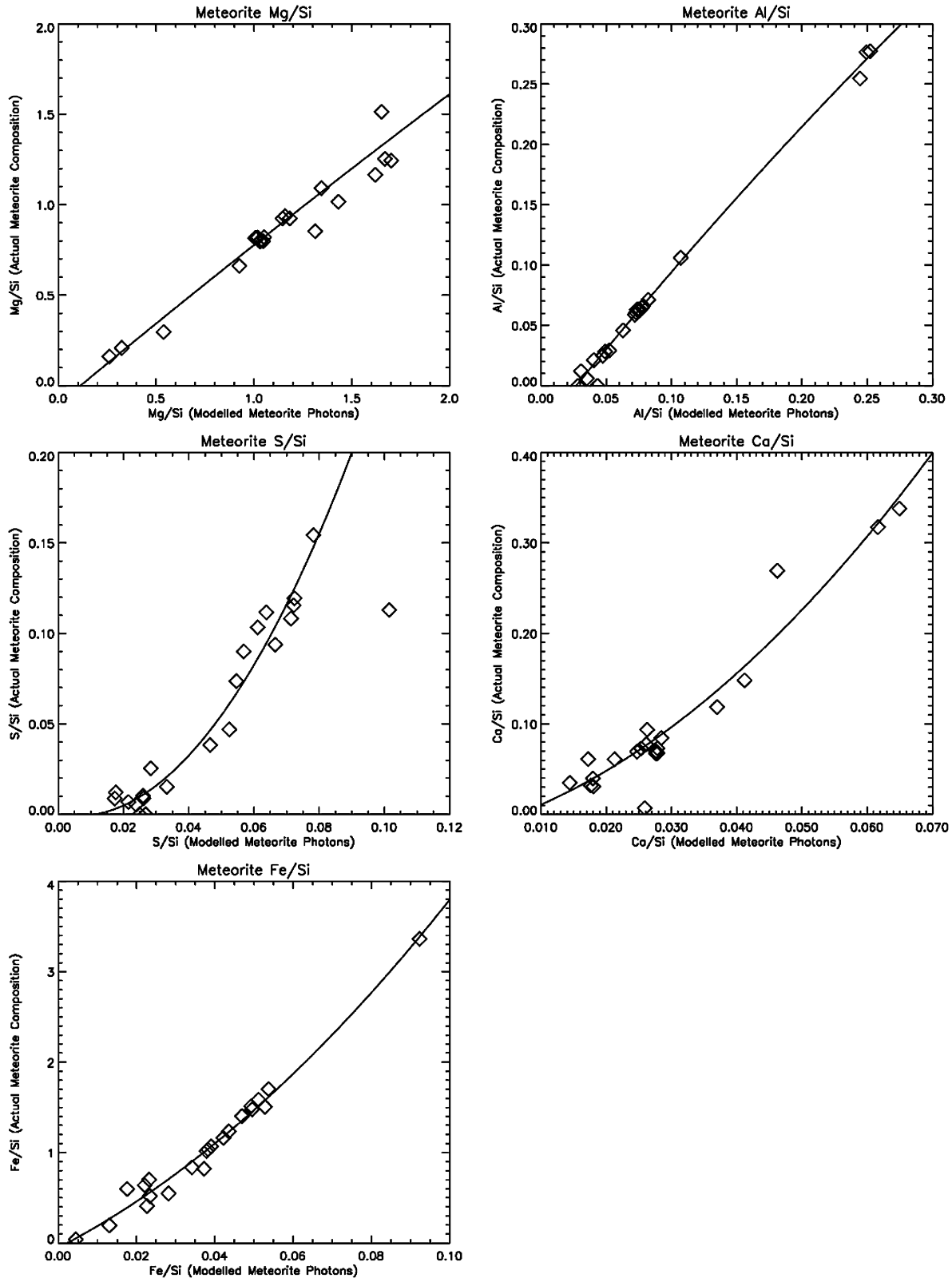
Fig. 6. Theoretical calibration curves based on a range of bulk meteorite compositions (diamond symbols; Nittler et al., 2004) and the solar spectrum and geometry appropriate for the solar flare observed on 17 June 2000. Curves are quadratic fits to the data and allow the derivation of elemental abundance ratios from X-ray line flux ratios observed from 433 Eros.

measured by NEAR. The measurements of the Fe/Si, Ca/Si, and S/Si fluorescent photon ratios, therefore, are subject to lower statistical uncertainties than for any other flare. However, because of the high off-normal angle ("panel angle") of the gas solar monitor with respect to the Sun ($\theta_{mean} = 35.5°$), the derivation of the solar spectrum for this flare (and therefore the conversion of the photon ratios from this flare to elemental abundance ratios) is also the most sensitive to the graded filter dimensions.

Table 8
Photon counts and ratios for eight solar flares.

Date (UT)	Flare METs	Photon counts					
		Mg	Al	Si	S	Ca	Fe
2000-May-04	MET 132826285-27185	15614 ± 451	1360 ± 469	17249 ± 362	830 ± 121	910 ± 71	1707 ± 59
2000-May-20	MET 134210436-12886	16815 ± 656	1492 ± 781	12799 ± 466	301 ± 161	56 ± 92	267 ± 69
2000-Jun-15	MET 136508736-10886	7386 ± 472	902 ± 380	7893 ± 380	154 ± 147	399 ± 90	665 ± 69
2000-Jun-17	MET 136620036-21786	5795 ± 401	417 ± 382	6458 ± 327	391 ± 134	205 ± 76	555 ± 58
2000-Jul-10	MET 138677136-80836	18449 ± 761	1293 ± 1176	16589 ± 529	510 ± 197	604 ± 118	457 ± 89
2000-Dec-27	MET 153341842-42742	11894 ± 405	303 ± 369	12440 ± 319	657 ± 113	642 ± 64	1426 ± 53
2000-Dec-28	MET 153418442-19292	10363 ± 398	1550 ± 380	9286 ± 273	373 ± 90	244 ± 54	342 ± 41
2001-Jan-02	MET 153832142-34142	11917 ± 476	1628 ± 476	12776 ± 385	170 ± 135	499 ± 81	876 ± 63
		Photon ratios					
		Mg/Si	Al/Si	S/Si	Ca/Si	Fe/Si	
2000-May-04	MET 132826285-27185	0.90 ± 0.03	0.079 ± 0.030	0.048 ± 0.007	0.05 ± 0.004	0.098 ± 0.004	
2000-May-20	MET 134210436-12886	1.31 ± 0.07	0.117 ± 0.061	0.023 ± 0.013	0.004 ± 0.007	0.021 ± 0.005	
2000-Jun-15	MET 136508736-10886	0.94 ± 0.07	0.114 ± 0.058	0.020 ± 0.019	0.051 ± 0.012	0.084 ± 0.010	
2000-Jun-17	MET 136620036-21786	0.90 ± 0.08	0.065 ± 0.059	0.061 ± 0.021	0.032 ± 0.012	0.086 ± 0.010	
2000-Jul-10	MET 138677136-80836	1.11 ± 0.06	0.078 ± 0.071	0.031 ± 0.012	0.036 ± 0.007	0.028 ± 0.005	
2000-Dec-27	MET 153341842-42742	0.96 ± 0.04	0.024 ± 0.030	0.053 ± 0.009	0.052 ± 0.005	0.115 ± 0.005	
2000-Dec-28	MET 153418442-19292	1.12 ± 0.05	0.167 ± 0.041	0.040 ± 0.010	0.026 ± 0.006	0.037 ± 0.005	
2001-Jan-02	MET 153832142-34142	0.93 ± 0.05	0.127 ± 0.037	0.013 ± 0.011	0.039 ± 0.006	0.069 ± 0.005	

Table 9
Composition results: Summary (average of data from eight solar flares).

	Uncorrected elemental ratios		Chondrites			Correction factors	Ratios with mineral-mixing correction applied	
			H	L	LL			
Mg/Si	0.753	+0.078/−0.055	0.82 ± 0.009	0.80 ± 0.009	0.80 ± 0.008	1.04 ± 0.08	0.783	+0.099/−0.081
Al/Si	0.069	+0.055/−0.055	0.066 ± 0.005	0.064 ± 0.052	0.062 ± 0.003	0.76 ± 0.05	0.052	+0.055/−0.055
S/Si	0.005	+0.008/−0.008	0.114 ± 0.009	0.114 ± 0.017	0.111 ± 0.022	1.34 ± 0.10	0.007	+0.008/−0.008
Ca/Si	0.060	+0.023/−0.024	0.072 ± 0.004	0.071 ± 0.004	0.072 ± 0.005	1.12 ± 0.10	0.067	+0.024/−0.025
Fe/Si	1.678	+0.338/−0.320	1.59 ± 0.068	1.18 ± 0.052	1.03 ± 0.046	1.42 ± 0.32	2.383	+0.635/−0.625

The solar monitor data for this flare and a representative model (here based on Model 5, Table 3) are plotted as Fig. 7a. Because the low-energy solar flux is almost entirely cut off from the pinhole in the thicker-Delrin model, the emission measure of the low-T component must be several times higher in order to account for the measured low-T flux than in the thin-Delrin model. Consequently, the thin-Delrin filter models imply a much harder solar X-ray spectrum than the thick-Delrin versions. This has a profound effect on the determination of the Fe/Si and Ca/Si ratios from the asteroid. If the thin-Delrin filter models are correct, the solar spectrum during this flare was quite hard, making it possible for a relatively low abundance of asteroidal iron to produce all the iron signal seen in the asteroid-pointing detectors. In this case, the Fe/Si abundance implied by the asteroid fluorescence would have been relatively low (Fe/Si = 2.07 ± 0.11 for Model 2; Table 11). On the other hand, if the thick-Delrin filter model is correct, the solar spectrum of this flare was much softer, requiring a higher abundance of iron in the asteroid in order for a relatively low number of hard solar X-rays to produce the iron signal detected by the NEAR XRS. Therefore, in this case the Fe/Si abundance ratio would have had to have been much higher: Fe/Si = 4.83 ± 0.27 for solar model 11. Ultimately, this means that the Fe/Si (and Ca/Si) results from this flare suffer from a large systematic uncertainty stemming entirely from uncertainty in the properties of the solar monitor graded filter, in spite of the good raw photon statistics from Fe and Ca.

6.2. 20 May 2000

The high-temperature component of the flare from May 20, 2000 (Fig. 7b) was relatively cool and weak compared with that of the other studied flares. This "softer" X-ray spectrum induced few iron counts from the asteroid, so the statistical uncertainty in the derived Fe/Si value is high. A favorable spacecraft geometry with respect to the asteroid, however, enabled significant Mg, Al, and Si

fluorescence to be measured by the asteroid-pointing detectors. As with the May 4, 2000 flare, a systematic uncertainty in the Al/Si photon ratio due to uncertainty in the Al-filtered detector zero is included in Table 8.

6.3. 15 June and 17 June 2000

Solar monitor data and corresponding model spectra from flares on June 15 and 17 of 2000 are shown in Figs. 7c and 7d, respectively. These two flares were very similar in both inferred solar temperature and geometry. The last calibration-source data between June and August 2000 were taken on 8 June 2000, so the calibration-based detector characteristics for these flares and the subsequent one on July 10 are increasingly uncertain. Based on the unfiltered detector solutions for these flares (Table 6) it would appear that no resolution-degrading event affected the asteroid-pointing detectors during this time period. Upper limits of 0.381 and 0.396 were assigned to the FWHM (resolution) parameters of the Mg- and Al-filtered detectors based on the 6–8 June calibration data.

As with the previous flares, the systematic uncertainty in the Al/Si photon ratio due to Al-filtered zero calibration has been included in Table 8. For the June 15 flare, the high (limited Al-detector zero) and low (floating zero point) values for Al/Si are 0.096 ± 0.058 and 0.054 ± 0.064, respectively. For the June 17 flare, the high- and low-Al/Si solutions are 0.046 ± 0.060 and 0.022 ± 0.065, respectively.

6.4. 10 July 2000

Solar monitor data and a model spectrum from the solar flare of July 10, 2000 are plotted as Fig. 7e. Although the solar panel angle for this flare was the lowest (closest to normal incidence) of those among the eight major solar flares, the χ^2 values of the solar
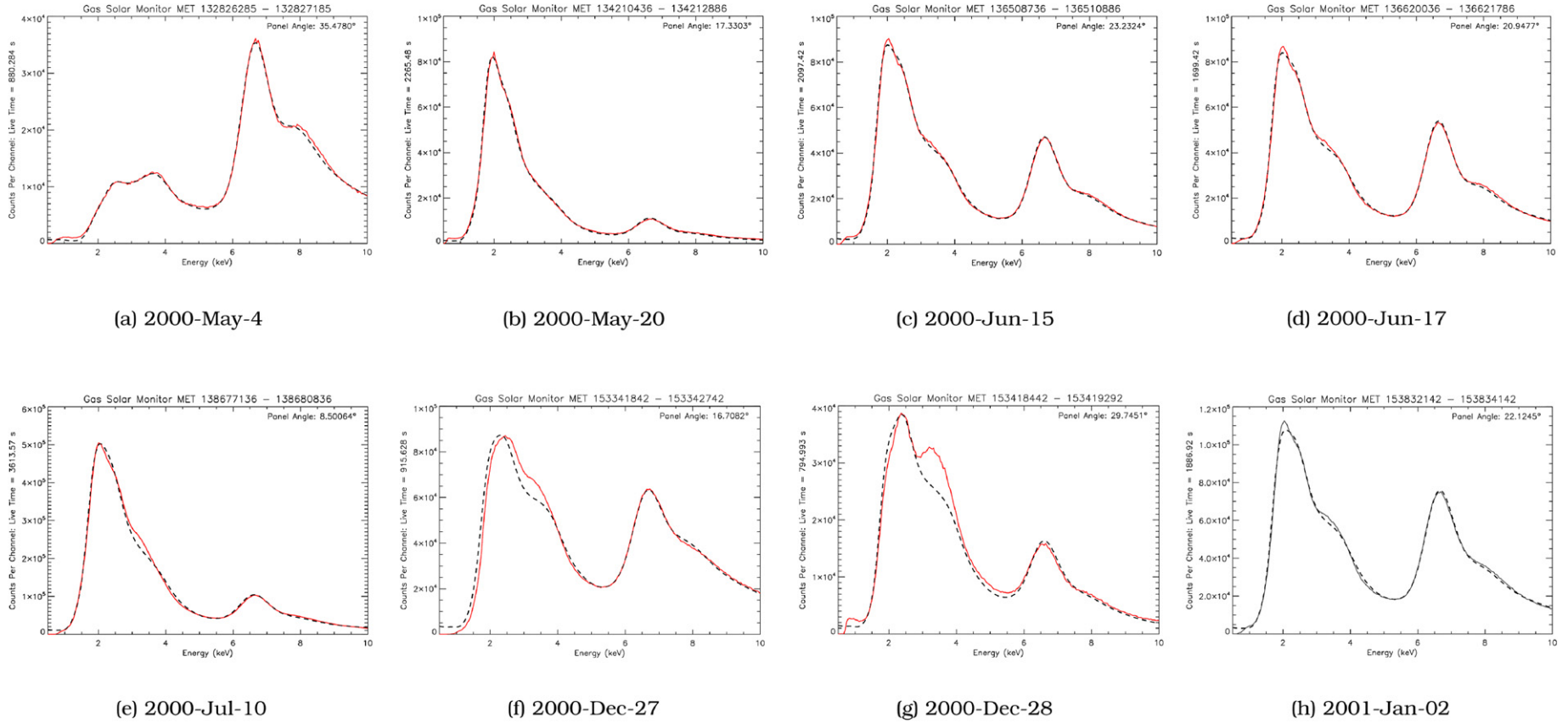
Fig. 7. Solar flares: Observed and modeled solar monitor spectra from eight solar flares for which fluorescence was observed from 433 Eros. For each flare, the solid line is the sum of all gas solar monitor spectra acquired during the solar flare, after each was individually corrected for zero shift; the dashed line is the sum of all the corresponding two-temperature model spectra (each 50-s integration having been modeled separately).

Table 10
Composition results: Effect of solar models on elemental ratios for 433 Eros. Each composition is the average of results from eight solar flares. No mineral-mixing correction has been applied.

	Elemental ratios, eight-flare averages				
	Mg/Si	Al/Si	S/Si	Ca/Si	Fe/Si
Model 1	0.746 ± 0.015	0.068 ± 0.018	0.0053 ± 0.0025	0.062 ± 0.007	1.680 ± 0.061
Model 2	0.749 ± 0.015	0.069 ± 0.018	0.0052 ± 0.0025	0.061 ± 0.007	1.652 ± 0.060
Model 3	0.760 ± 0.015	0.069 ± 0.018	0.0052 ± 0.0025	0.062 ± 0.007	1.715 ± 0.059
Model 4	0.746 ± 0.015	0.068 ± 0.018	0.0051 ± 0.0025	0.062 ± 0.007	1.754 ± 0.062
Model 5	0.761 ± 0.015	0.070 ± 0.018	0.0051 ± 0.0025	0.060 ± 0.007	1.661 ± 0.058
Model 6	0.756 ± 0.015	0.069 ± 0.018	0.0049 ± 0.0025	0.059 ± 0.007	1.818 ± 0.066
Model 7	0.743 ± 0.015	0.068 ± 0.018	0.0050 ± 0.0025	0.061 ± 0.007	1.786 ± 0.065
Model 8	0.747 ± 0.015	0.068 ± 0.018	0.0051 ± 0.0025	0.062 ± 0.007	1.730 ± 0.061
Model 9	0.745 ± 0.015	0.068 ± 0.018	0.0051 ± 0.0025	0.060 ± 0.007	1.591 ± 0.061
Model 10	0.783 ± 0.016	0.070 ± 0.018	0.0045 ± 0.0024	0.054 ± 0.006	1.528 ± 0.054
Model 11	0.743 ± 0.015	0.068 ± 0.018	0.0050 ± 0.0025	0.059 ± 0.007	1.541 ± 0.061

Table 11
Composition results: Individual solar flares. The model number(s) of the graded filter model (Table 3) is given in parentheses following the corresponding ratio.

	Mg/Si		Al/Si		S/Si		Ca/Si		Fe/Si	
					2000-May-4					
Max.	0.685 ± 0.028	(3)	0.065 ± 0.039	(3, 5)	0.037 ± 0.014	(11)	0.299 ± 0.047	(11)	4.83 ± 0.27	(11)
Min.	0.659 ± 0.028	(9)	0.062 ± 0.038	(11, 9)	0.026 ± 0.010	(10)	0.151 ± 0.047	(3)	2.07 ± 0.11	(3)
Average	0.671 ± 0.031		0.064 ± 0.039		0.031 ± 0.013		0.214 + 0.091/−0.071		3.11 + 1.73/−1.06	
					2000-May-20					
Max.	0.953 ± 0.050	(10)	0.100 ± 0.072	(10)	0.010 ± 0.015	(11, 2, 1)	0.020 ± 0.011	(3)	3.04 ± 1.04	(7)
Min.	0.879 ± 0.046	(11)	0.093 ± 0.069	(9)	0.026 ± 0.010	(10)	0.017 ± 0.010	(10)	2.47 ± 0.81	(10)
Average	0.905 + 0.068/−0.054		0.095 ± 0.070		0.009 ± 0.014		0.019 ± 0.012		2.87 + 0.99/−1.06	
					2000-Jun-15					
Max.	0.704 ± 0.063	(10)	0.059 ± 0.082	(10)	0.004 ± 0.010	(sev.)	0.318 ± 0.138	(7)	4.21 ± 0.65	(7)
Min.	0.631 ± 0.057	(11)	0.053 ± 0.038	(7)	0.003 ± 0.010	(sev.)	0.227 ± 0.097	(10)	3.30 ± 0.11	(10)
Average	0.650 + 0.080/−0.062		0.055 ± 0.079		0.004 ± 0.010		0.295 + 0.129/−0.144		3.93 + 0.66/−0.86	
					2000-Jun-17					
Max.	0.671 ± 0.066	(10)	0.023 ± 0.082	(10)	0.061 ± 0.049	(1, 7)	0.092 ± 0.058	(7)	3.13 ± 0.22	(7)
Min.	0.605 ± 0.061	(11)	0.020 ± 0.038	(sev.)	0.050 ± 0.010	(10)	0.071 ± 0.044	(10)	2.47 ± 0.44	(10)
Average	0.628 + 0.076/−0.067		0.021 ± 0.074		0.059 ± 0.048		0.087 + 0.055/−0.057		2.91 + 0.52/−0.64	
					2000-Jul-10					
Max.	0.861 ± 0.048	(10)	0.061 ± 0.065	(sev.)	0.010 ± 0.011	(sev.)	0.126 ± 0.046	(3)	1.35 ± 0.28	(3)
Min.	0.847 ± 0.047	(3)	0.060 ± 0.064	(sev.)	0.009 ± 0.010	(sev.)	0.102 ± 0.036	(10)	1.14 ± 0.24	(11)
Average	0.852 ± 0.048		0.060 ± 0.064		0.010 ± 0.011		0.116 ± 0.044		1.26 + 0.28/−0.29	
					2000-Dec-27					
Max.	0.930 ± 0.042	(10)	0.0 ± 0.037	(all)	0.022 ± 0.009	(3)	0.067 ± 0.011	(3)	1.42 ± 0.08	(3)
Min.	0.903 ± 0.041	(3)	0.0 ± 0.037	(all)	0.019 ± 0.008	(10)	0.056 ± 0.009	(10)	1.19 ± 0.07	(11)
Average	0.912 + 0.048/−0.043		0.0 ± 0.037		0.021 ± 0.009		0.062 ± 0.012		1.32 + 0.12/−0.15	
					2000-Dec-28					
Max.	0.839 ± 0.045	(10, 3)	0.159 ± 0.050	(10)	0.023 ± 0.015	(11)	0.090 ± 0.037	(11)	7.03 ± 1.35	(11)
Min.	0.835 ± 0.044	(11, 7, 9)	0.156 ± 0.049	(6, 7, 9)	0.021 ± 0.013	(sev.)	0.078 ± 0.032	(3)	5.29 ± 0.98	(3)
Average	0.837 ± 0.045		0.157 ± 0.049		0.022 ± 0.014		0.083 ± 0.035		5.91 + 1.58/−1.28	
					2001-Jan-02					
Max.	0.702 ± 0.041	(10)	0.122 ± 0.050	(10)	0.0 ± 0.003	(all)	0.114 ± 0.032	(7)	2.23 ± 0.24	(7)
Min.	0.619 ± 0.037	(7)	0.113 ± 0.049	(7)	0.0 ± 0.003	(all)	0.086 ± 0.024	(10)	1.75 ± 0.19	(10)
Average	0.639 + 0.074/−0.043		0.116 ± 0.044		0.0 ± 0.003		0.107 + 0.031/−0.036		2.073 + 0.28/−0.40	

spectral fitting remain relatively high regardless of the graded filter characteristics. The χ^2 improves with degraded gas solar monitor resolution, suggesting that this detector's resolution had been degraded somewhat from its near-optimal values during the previous solar flares. Fortunately, the effect of degraded solar monitor resolution on the geochemical results is much less than the uncertainty due to the statistical errors in the photon counts. Since no ^{55}Fe calibration data had been taken for over a month at the time of this flare, no limits on the zero points of the asteroid-pointing detectors were applied. The best-fit flare-derived resolution parameters of the asteroid-pointing detectors were 0.360, 0.373, and 0.439 for the unfiltered, Mg-filtered, and Al-filtered detectors respectively. Applying an upper limit of 0.390 to the Al-filtered detector resolution (on the assumption that it usually did not stray too far from

the resolution of the unfiltered detector) did not materially change the photon ratios.

6.5. 27 December 2000

This flare was unusual in that its solar monitor data could not be fit satisfactorily with any of the usual sets of solar elemental abundances (Meyer, 1985; Feldman et al., 1992), or the "Coronal 1" and "Coronal 2" sets that produced good matches to numerous other NEAR flares; see Table 1). The 6.5 keV iron emission structure was less prominent with respect to the bremsstrahlung continuum than was permitted by these models. Additional sets of abundances were tested: some with overall metallicity decreased further below the estimate of Meyer (1985), so that the relationships between el-

ements other than H and He were unchanged; and some with the iron abundance reduced alone. The best fits were produced with only the Fe abundance reduced, and the best-performing abundance model out of the reduced-iron set (Fe/H = 1.95×10^{-5}, as opposed to the Meyer (1985) value Fe/H = Si/H = 3.9×10^{-5}) was adopted. This model is "Coronal 3" in Table 1. We note that flare-to-flare variability of at least this magnitude in both the Fe/Ca ratio and the Fe/H ratio has previously been observed (Antonucci and Martin, 1995; Fludra and Schmelz, 1999). The actual and modelled solar monitor data are plotted in Fig. 7f.

The solar monitor gain during this and all subsequent flares was 0.0415 keV/channel, an increase from the 0.040 keV/channel that had consistently been observed during the summer flares. This may have been caused by space charge effects or other consequences of detector aging. The asteroid-pointing detectors were unaffected, probably because they had counted far fewer X-rays during the course of the mission.

6.6. 28 December 2000

The December 28 flare was not analyzed by Nittler et al. (2001), largely because the solar spectrum could not be modelled satisfactorily at that time. The CHIANTI 5.2 code yields reasonable models with both the "Coronal 1" and "Coronal 2" coronal abundance models.

However, the modelling (Fig. 7g) remains less successful than with most of the other flares, largely because of a very large excess of counts at about 3.5 keV. Because of the attenuation of the low-energy photons by the graded filter, the gas solar monitor is vastly more sensitive at 3.5 keV than it is at 2 keV. Thus, a large number of measured counts at 3.5 keV actually represents far fewer incident solar photons than a corresponding number at 2 keV, and affects the resulting asteroid composition relatively little. For this reason, while fitting this flare, the region between 2.72 and 3.44 keV was eliminated from the χ^2 calculation altogether, so that the fits in the 2 keV and 6.5 keV regions that are more important to X-ray production in the asteroid would be undistorted. The origin of the excess signal at 3.5 keV remains unknown, though we note it cannot easily be explained by an increase in the solar K or Ar abundances in the flaring plasma, as the required enrichment factors ($>60\times$ for K, $>5\times$ for Ar) are implausible.

The photon ratios in the asteroid-pointing detectors for this flare, unlike those for the May 4 flare, are insensitive to restrictions on the asteroid-pointing detector parameters.

6.7. 2 January 2001

The solar spectra from the 2 January 2001 flare were easily fitted with the coronal-abundance solar spectral models, lacking either the 3 keV excess of the December 28 flare or the deficit of iron emission in the December 27 flare.

The solar monitor gain during this flare was 0.0415 keV/channel. The FWHM parameter of the gas solar monitor was increased by 8%. (Fitting with the degraded resolution reduced the χ^2 of the solar monitor fitting, but the geochemical results were unchanged when the solar fits were done with the standard resolution (FWHM parameter = 0.340).) The integrated data from and models of gas solar monitor output are plotted as Fig. 7h.

7. Results and discussion

Table 10 illustrates the effect of the uncertainties in the solar X-ray spectra on the derived composition of 433 Eros. For each solar model, Table 10 lists the weighted average of the composition ratios derived from all eight solar flares. These element ratios are
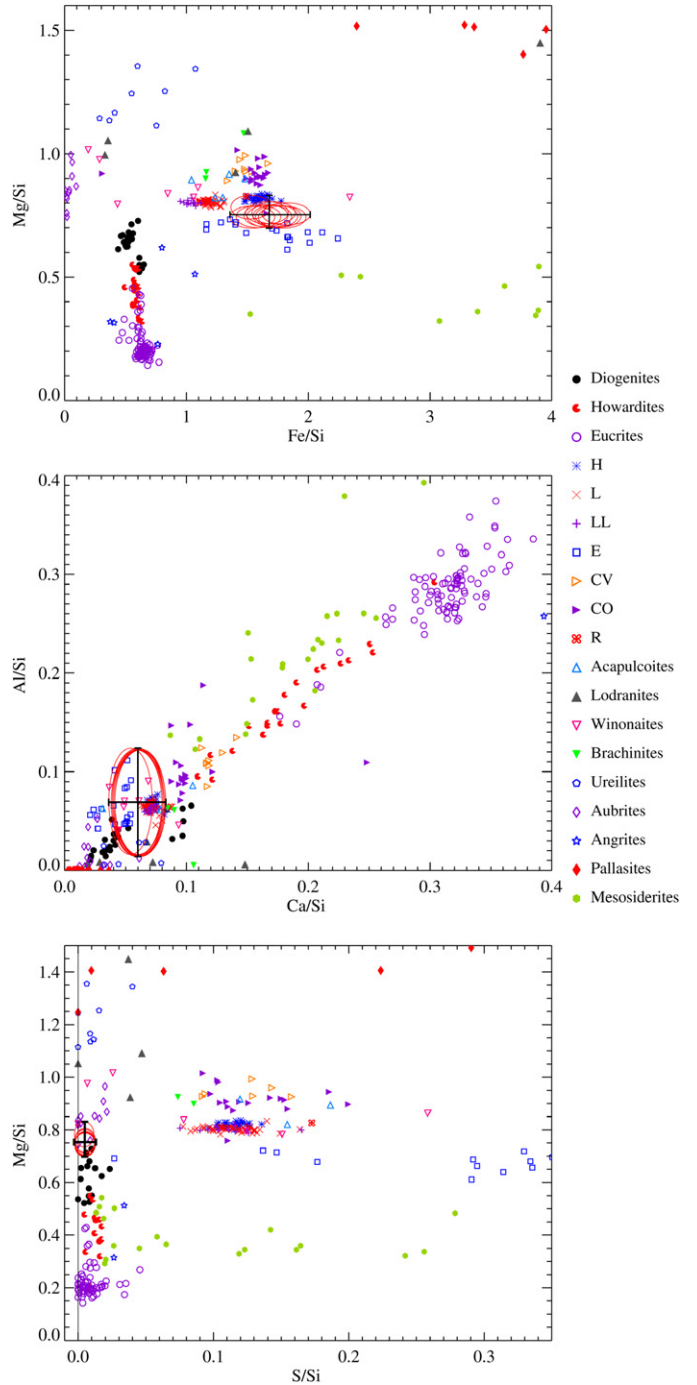

Fig. 8. XRS-derived elemental ratios for 433 Eros in the context of bulk compositions of various meteorite classes. Ellipses represent 3σ uncertainties in average compositions as calculated using individual solar models (Tables 3 and 10). No mineral-mixing correction (cf. Foley et al., 2006; Nittler et al., 2001) has been applied. Uncertainties in the final results (large crosshairs) combine uncertainties in the solar model with those due to photon statistics from the asteroid's fluorescence. These data are tabulated in Table 9. Top: Mg/Si vs Fe/Si. Middle: Al/Si vs Ca/Si. Bottom: Mg/Si vs S/Si.

represented by the 3σ error ellipses in Fig. 8. No correction for mineral-mixing effects has been applied to these values.

Results for each solar flare are individually represented in Table 11. For each elemental ratio derived from each flare, the maximum and minimum values from among the solar models are tabulated. The average value for that flare from all the solar models follows. The systematic errors due to solar uncertainties are estimated from the maximum and minimum values derived from
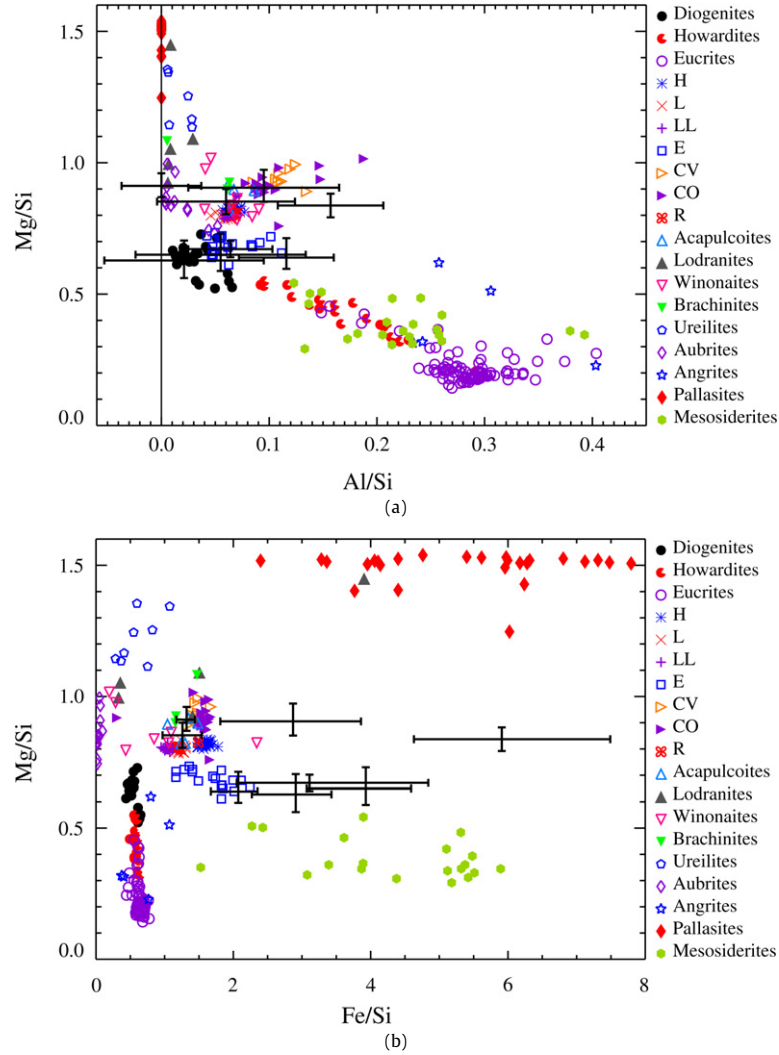
Fig. 9. Flare-to-flare variation in XRS-derived elemental ratios for 433 Eros in the context of bulk meteorite compositions. Error bars represent 1σ uncertainties in each of the eight single-flare compositions, including uncertainties due to uncertainties in the solar spectra. These data are also tabulated in Table 11.

the various solar models; these have been combined in a root-summed-square sense with the independent random errors due to photon statistics. (The standard deviation would not be an accurate reflection of the uncertainties due to the solar uncertainties because the set of models included is not a random sample of all plausible solar models.)

Table 9 presents the overall composition results of this work, averaged over all eight solar flares and including errors due to uncertainties in the solar flare spectra. The first column ("uncorrected") lists the compositions without any correction applied for mineral-mixing effects. These data are also represented as the large crosshairs in Fig. 8. The final column has had the mineral-mixing corrections applied as in Nittler et al. (2001) and may therefore be directly compared with the results from that paper. For comparison, the average compositions of the H, L, and LL chondrites from the compilation of Nittler et al. (2004) are also shown.

Plotted in Fig. 9 are the Mg/Si, Al/Si, and Fe/Si ratios calculated from the eight individual solar flares, illustrating the flare-to-flare variability of the data. Each set of crosshairs represents the 1σ uncertainty in composition for a single flare, including both errors due to counting statistics and those propagated from the uncertainties in the solar spectra. Although the range of element ratios determined from the different flares at first glance might appear to indicate compositional heterogeneity for Eros, in fact no one flare

is more than 3σ away from each other or the ordinary chondrite field in Mg/Si or Al/Si. The flare-to-flare variability of Fe/Si is larger but, as discussed below, this ratio is subject to additional systematic errors not related to solar modeling. Thus, the XRS data alone can neither establish nor eliminate the possibility of spatial variation on 433 Eros.

However, the NEAR MSI/NIS investigation (Veverka et al., 2000; Bell et al., 2002) has provided strong evidence for compositional homogeneity over all of Eros, and the chondritic Cr/Fe ratio that has been derived from the XRS data (Foley et al., 2006) also supports the hypothesis that Eros is an undifferentiated object with a chemical affinity to the ordinary chondrites. The averaged composition in Fig. 8, therefore, probably represents the light-element composition of the whole of Eros.

The composition ratios derived from individual flares have changed somewhat since the XRS analysis of Nittler et al. (2001), but the overall averages are mostly similar to the "Best Eros" values quoted by Nittler et al. Of particular importance, the sulfur/silicon ratio remains substantially below those of chondritic meteorites. Trombka et al. (2000) and Nittler et al. (2001) suggested that the sulfur deficiency could be caused by either space weathering processes (e.g., sputtering, impact vaporization) or partial differentiation with loss of a S-rich melt. Foley et al. (2006) determined a chondritic Cr/Fe ratio for Eros based on XRS data from two solar flares and argued on the basis of this that space
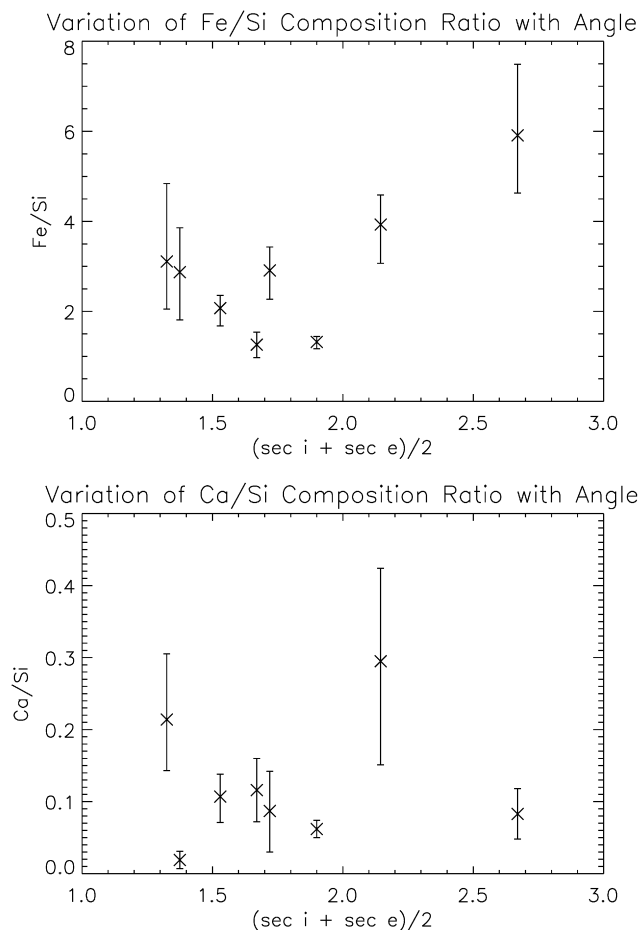
Fig. 10. Variation of Fe/Si and Ca/Si with observing geometry. sec i is the average secant of the incidence (off-normal) angle of the illumination of the portion of 433 Eros within the field of view of the NEAR XRS during each solar flare; sec e is the corresponding emission angle. The data point with the highest Fe/Si ratio and highest (sec i + sec e) corresponds to the solar flare of 28 December 2000; however the Ca/Si derived from the same flare is chondritic.

weathering must be responsible for the sulfur deficiency since partial melting should also deplete chromium. Optical space weathering (Pieters et al., 2000; Hapke, 2001; Sasaki et al., 2001) is caused by nanophase reduced iron production and deposition on grain surfaces. The MSI/NIS measurements (Clark et al., 2001) established that the spectrum of Eros has been altered by space weathering. The same processes responsible for nanophase iron production, such as sputtering and impact vaporization, likely also vaporize sulfur and cause sulfur depletion in the surface layers (e.g., Nittler et al., 2001; Killen, 2003; Kracher and Sears, 2005).

The new average Fe/Si ratio is slightly higher than that of Nittler et al. (2001), but most H chondrites fall within its 1σ error ellipse. As discussed previously (e.g., McCoy et al., 2001), however, the NEAR gamma-ray spectrometer (GRS)-derived Fe/Si ratio of 0.8 ± 0.3 (Evans et al., 2001) is considerably lower than the XRS derived Fe/Si and more consistent with the low-iron ordinary chondrite groups L and LL. Since the GRS samples to depths of tens of centimeters, whereas the X-rays originate from the top tens to hundreds of microns, this difference suggests that the elevated Fe/Si is a surface phenomenon. However, there are several additional difficulties beyond solar modeling in determining Eros' Fe/Si ratio from XRS data, as discussed below.

Okada (2002, 2004) has suggested that the large phase angle of the NEAR XRS observations should lead to erroneously high Fe/Si ratios due to shadowing effects. For example, in laboratory experiments, Okada (2002, 2004) demonstrated that for ground basalt samples sieved to various particle sizes, the ratios of Ca/Fe and Ti/Fe K lines decrease significantly as the phase angle of observation increases. These authors also demonstrated that this effect becomes much more important as the size of the sieved particles increases. Okada (2002) concluded that the magnitude of this angular effect increases with the energy difference between the K lines that are being compared and the effect on Si/Fe (Si $K_\alpha = 1.74$ keV) should thus be even more pronounced than the observed effects on Ca/Fe and Ti/Fe.

Fig. 10 illustrates an attempt to explore possible geometric effects on the Fe/Si and Ca/Si results, not through phase angle (since all the NEAR data had approximately the same phase angle) but by plotting composition results from individual solar flares against a "path length parameter" which is a function of incidence and emission angle. This parameter, which is the sum of the secant of the incidence angle and the secant of the emission angle, represents the path traveled by incoming and outgoing X-rays through the overburden of soil above the fluorescing atom. One would expect matrix effects to increase as this parameter increases. The figure shows that the two highest single-flare Fe/Si values do come from the flares with the highest values of the path length parameter. However, the Ca/Si result from the highest path-length flare (28 December) is apparently not inflated by this geometric effect.

Another effect that may be important in interpreting the NEAR data is size sorting in the regolith due either to the "Brazil nut" effect (Rosato et al., 1987) or to the reverse Brazil nut effect (Hong et al., 2001). If the mineral grains in which Fe is carried have different physical properties than the low-Fe regolith grains (e.g., metal versus silicate), size sorting in the regolith could alter the Fe/Si at the surface.

Thus, given the dependence of the measured Fe/Si ratio on uncertainties in the solar spectrum, on phase angle effects and on the possibility of surface or regolith processes, the flare-to-flare variability in Fe/Si shown in Fig. 9 is much more likely a reflection of systematic errors rather than of true elemental heterogeneity on the asteroid. As discussed earlier, the observed spatial homogeneity in surface colors and mineralogy (based on MSI/NIS data) and the light-element XRS results all point to Eros being an undifferentiated asteroid.

Overall, the two-temperature model was successful in modeling the 1–10 keV NEAR solar X-ray spectra. This approach may be useful in the analysis of data from the Hayabusa XRS (Okada et al., 2006), particularly in the determination of the S/Si ratio of 25143 Itokawa (or an upper limit thereof) since Hayabusa's onboard standard sample plate lacked sulfur (Okada et al., 2006). This will enable comparison of Itokawa's S/Si value with Eros' highly depleted S/Si. This approach may also be helpful in analysis of Mercury data from the MESSENGER XRS (X-ray spectrometer; Gold et al., 2001) which is an improved version of the NEAR XRS design. Although the energy resolution of the Si-PIN solar monitor carried by the MESSENGER XRS is significantly improved from that of the NEAR gas counter, it is still insufficient to resolve the closely spaced solar emission lines in the region of the K-edges of the light elements Mg, Al, Si, and S. Thus, it will be necessary to use CHIANTI or a similar method of modeling the solar X-ray spectrum in conjunction with the solar monitor data in order to obtain quantitative compositional results from the MESSENGER XRS.

construction of the gas solar monitor. We also express our appreciation to Ken Phillips for advice on solar physics and the CHIANTI code. Finally, we wish to thank K. Joy and T. Okada for their helpful reviews.

References

Acton, L.W., Finch, M.L., Gilbreth, C.W., Culhane, J.L., Bentley, R.D., Bowles, J.A., Guttridge, P., Gabriel, A.H., Firth, J.G., Hayes, R.W., 1980. The soft X-ray polychromator for the solar maximum mission. Sol. Phys. 65, 53–71.

Antonucci, E., Dodero, M.A., 1995. Temperature dependence of nonthermal motions in solar flare plasmas observed with the flat crystal spectrometer on SMM. Astophys. J. 438, 480–490.

Antonucci, E., Martin, R., 1995. Differential emission measure and iron-to-calcium abundance in solar flare plasmas. Astrophys. J. 451, 402–412.

Bell, J.F., Izenberg, N.I., Lucey, P.G., Clark, B.E., Peterson, C., Gaffey, M.J., Joseph, J., Carcich, B., Harch, A., Bell, M.E., Warren, J., Martin, P.D., McFadden, L.A., Wellnitz, D., Murchie, S., Winter, M., Veverka, J., Thomas, P., Robinson, M.S., Malin, M., Cheng, A., 2002. Near-IR reflectance spectroscopy of 433 Eros from the NIS instrument on the NEAR mission. I. Low phase angle observations. Icarus 155, 119–144.

Buseck, P.R., 1977. Pallasite meteorites—Mineralogy, petrology and geochemistry. Geochim. Cosmochim. Acta 41, 711–721.

Cheng, A.F., 1997. Near Earth Asteroid Rendezvous: Mission overview. Space Sci. Rev. 82, 3–29.

Clark, B.E., Lucey, P., Helfenstein, P., Bell, J.F., Peterson, C., Veverka, J., McConnochie, T., Robinson, M.S., Bussey, B., Murchie, S.L., Izenberg, N.I., Chapman, C.R., 2001. Space weathering on Eros: Constraints from albedo and spectral measurements of Psyche crater. Meteorit. Planet. Sci. 36, 1617–1637.

Clark, P.E., Trombka, J., Floyd, S., 1995, Solar monitor design for the NEAR X-ray spectrometer. Lunar Planet. Sci. XXVI, 253–254.

Dere, K.P., Landi, E., Mason, H.E., Monsignori Fossi, B.C., Young, P.R., 1997. CHIANTI—An atomic database for emission lines. Astron. Astrophys. Suppl. 125, 149–173.

Dyakonova, M.I., Kharitonova, V.X., 1961. Meteoritika 21, 52 (Russian).

Evans, L.G., Starr, R.D., Brückner, J., Reedy, R.C., Boynton, W.V., Trombka, J.I., Goldstein, J.O., Masarik, J., Nittler, L.R., McCoy, T.J., 2001. Elemental composition from gamma-ray spectroscopy of the NEAR-Shoemaker landing site on 433 Eros. Meteorit. Planet. Sci. 36, 1639–1660.

Feldman, U., Mandelbaum, P., Seely, J.F., Doschek, G.A., Gursky, H., 1992. The potential for plasma diagnostics from stellar extreme-ultraviolet observations. Astophys. J. Suppl. 81, 387–408.

Feldman, U., Doschek, G.A., Mariska, J.T., Brown, C.M., 1995. Relationships between temperature and emission measure in solar flares determined from highly ionized iron spectra and from broadband X-ray detectors. Astophys. J. 450, 441–449.

Fludra, A., Schmelz, J.T., 1999. The absolute coronal abundances of sulfur, calcium, and iron from Yohkoh-BCS flare spectra. Astron. Astrophys. 348, 286–294.

Foley, C.N., 2002. Mars pathfinder alpha proton X-ray spectrometer calibration, data analyses, and interpretation. Ph.D. thesis, University of Chicago.

Foley, C.N., Nittler, L.R., McCoy, T.J., Lim, L.F., Brown, M.R.M., Starr, R.D., Trombka, J.I., 2006. Minor element evidence that Asteroid 433 Eros is a space-weathered ordinary chondrite parent body. Icarus 184, 338–343.

Garcia, H.A., 1994. Temperature and emission measure from GOES soft X-ray measurements. Sol. Phys. 154, 275–308.

Gold, R.E., Solomon, S.C., McNutt, R.L., Santo, A.G., Abshire, J.B., Acuñā, M.H., Afzal, R.S., Anderson, B.J., Andrews, G.B., Bedini, P.D., Cain, J., Cheng, A.F., Evans, L.G., Feldman, W.C., Follas, R.B., Gloeckler, G., Goldsten, J.O., Hawkins, S.E.I., Izenberg, N.R., Jaskulek, S.E., Ketchum, E.A., Lankton, M.R., Lohr, D.A., Mauk, B.H., McClintock, W.E., Murchie, S.L., Schlemm II, C.E., Smith, D.E., Starr, R.D., Zurbuchen, T.H., 2001. The MESSENGER mission to Mercury: Scientific payload. Planet. Space Sci. 49, 1467–1479.

Goldsten, J.O., McNutt, R.L., Gold, R.E., Gary, S.A., Fiore, E., Schneider, S.E., Hayes, J.R., Trombka, J.I., Floyd, S.R., Boynton, W.V., Bailey, S., Brueckner, J., Squyres, S.W., Evans, L.G., Clark, P.E., Starr, R., 1997. The X-ray/gamma-ray spectrometer on the Near Earth Asteroid Rendezvous Mission. Space Sci. Rev. 82, 169–216.

Grevesse, N., Sauval, A.J., 1998. Standard solar composition. Space Sci. Rev. 85, 161–174.

Hapke, B., 2001. Space weathering from Mercury to the asteroid belt. J. Geophys. Res. 15, 10039–10074.

Hong, D.C., Quinn, P.V., Luding, S., 2001. Reverse Brazil nut problem: Competition between percolation and condensation. Phys. Rev. Lett. 86, 3423–3426.

Hubbell, J.H., 1997. Summary of existing information on the incoherent scattering of photons, particularly on the validity of the use of the incoherent scattering function. Radiat. Phys. Chem. 50, 113–124.

Jarosewich, E., 1990. Chemical analyses of meteorites—A compilation of stony and iron meteorite analyses. Meteoritics 25, 323–337.

Kepa, A., Sylwester, J., Sylwester, B., Siarkowski, M., Stepanov, A.I., 2006. Determination of differential emission measure from X-ray solar spectra registered by RESIK aboard CORONAS-F. Solar Syst. Res. 40, 294–301.

Killen, R.M., 2003. Depletion of sulfur on the surface of asteroids and the Moon. Meteorit. Planet. Sci. 38, 383–388.

Kracher, A., Sears, D.W.G., 2005. Space weathering and the low sulfur abundance of Eros. Icarus 174, 36–45.

Landi, E., Del Zanna, G., Young, P.R., Dere, K.P., Mason, H.E., Landini, M., 2006. CHIANTI—An atomic database for emission lines. VII. New data for X-rays and other improvements. Astophys. J. Suppl. 162, 261–280.

Lin, R.P., Dennis, B.R., Hurford, G.J., Smith, D.M., Zehnder, A., Harvey, P.R., Curtis, D.W., Pankow, D., Turin, P., Bester, M., Csillaghy, A., Lewis, M., Madden, N., van Beek, H.F., Appleby, M., Raudorf, T., McTiernan, J., Ramaty, R., Schmahl, E., Schwartz, R., Krucker, S., Abiad, R., Quinn, T., Berg, P., Hashii, M., Sterling, R., Jackson, R., Pratt, R., Campbell, R.D., Malone, D., Landis, D., Barrington-Leigh, C.P., Slassi-Sennou, S., Cork, C., Clark, D., Amato, D., Orwig, L., Boyle, R., Banks, I.S., Shirey, K., Tolbert, A.K., Zarro, D., Snow, F., Thomsen, K., Henneck, R., Mchedlishvili, A., Ming, P., Fivian, M., Jordan, J., Wanner, R., Crubb, J., Preble, J., Matranga, M., Benz, A., Hudson, H., Canfield, R.C., Holman, G.D., Crannell, C., Kosugi, T., Emslie, A.G., Vilmer, N., Brown, J.C., Johns-Krull, C., Aschwanden, M., Metcalf, T., Conway, A., 2002. The Reuven Ramaty High-Energy Solar Spectroscopic Imager (RHESSI). Sol. Phys. 210, 3–32.

McCoy, T.J., Burbine, T.H., McFadden, L.A., Starr, R.D., Gaffey, M.J., Nittler, L.R., Evans, L.G., Izenberg, N., Lucey, P., Trombka, J.I., Bell, J.F., Clark, B.E., Clark, P.E., Squyres, S.W., Chapman, C.R., Boynton, W.V., Veverka, J., 2001. The composition of 433 Eros: A mineralogical–chemical synthesis. Meteorit. Planet. Sci. 36, 1661–1672.

McTiernan, J.M., Fisher, G.H., Li, P., 1999. The solar flare soft X-ray differential emission measure and the Neupert effect at different temperatures. Astophys. J. 514, 472–483.

Meyer, J.-P., 1985. Solar–stellar outer atmospheres and energetic particles, and galactic cosmic rays. Astophys. J. Suppl. 57, 173–204.

Moseley, H.G.J., 1913. The high-frequency spectra of the elements. Part I. Philos. Mag. 26, 1024–1034.

Nagahara, H., Ozawa, K., 1986. Petrology of Yamato-791493, "lodranite": Melting, crystallization cooling history, and relationship to other meteorites. Natl. Inst. Polar Res. Mem. 41, 181.

Nittler, L.R., Starr, R.D., Lim, L., McCoy, T.J., Burbine, T.H., Reedy, R.C., Trombka, J.I., Gorenstein, P., Squyres, S.W., Boynton, W.V., McClanahan, T.P., Bhangoo, J.S., Clark, P.E., Murphy, M.E., Killen, R., 2001. X-ray fluorescence measurements of the surface elemental composition of Asteroid 433 Eros. Meteorit. Planet. Sci. 36, 1673–1695.

Nittler, L.R., McCoy, T.J., Clark, P.E., Murphy, M.E., Trombka, J.I., Jarosewich, E., 2004. Bulk element compositions of meteorites: A guide for interpreting remote-sensing geochemical measurements of planets and asteroids. Antarctic Meteorite Res. 17, 231–251.

Okada, T., 2002. Surface elemental composition of Asteroid 433 Eros: Discussions on the results of the NEAR/XGRS. In: Proc. 35th ISAS Lunar Planetary Symposium, pp. 120–123.

Okada, T., 2004. Particle size effect in X-ray fluorescence at a large phase angle: Importance on elemental analysis of Asteroid Eros (433). Lunar Planet. Sci XXXV, 1927.

Okada, T., Shirai, K., Yamamoto, Y., Arai, T., Ogawa, K., Hosono, K., Kato, M., 2006. X-ray fluorescence spectrometry of Asteroid Itokawa by Hayabusa. Science 312, 1338–1341.

Phillips, K.J.H., 2004. The solar flare 3.8–10 keV X-ray spectrum. Astophys. J. 605, 921–930.

Pieters, C.M., Taylor, L.A., Noble, S.K., Keller, L.P., Hapke, B., Morris, R.V., Allen, C.C., McKay, D.S., Wentworth, S., 2000. Space weathering on asteroids: A mystery resolved with lunar samples. Meteorit. Planet. Sci. 35, 1101–1107. Supplement, p. A127.

Rosato, A., Strandburg, K.J., Prinz, F., Swendsen, R.H., 1987. Why the Brazil nuts are on top: Size segregation of particulate matter by shaking. Phys. Rev. Lett. 58, 1038–1040.

Sasaki, S., Nakamura, K., Hamabe, Y., Kurahashi, E., Hiroi, T., 2001. Production of iron nanoparticles by laser irradiation in a simulation of lunar-like space weathering. Nature 410, 555–557.

Schwartz, R.A., 1998. Version 6 of goes_transfer.pro.

Starr, R., Clark, P.E., Murphy, M.E., Floyd, S.R., McClanahan, T.P., Nittler, L.R., Trombka, J.I., Evans, L.G., Boynton, W.V., Bailey, S.H., Bhangoo, J., Mikheeva, I., Brückner, J., Squyres, S.W., McCartney, E.M., Goldsten, J.O., McNutt, R.L., 2000. Instrument calibrations and data analysis procedures for the NEAR X-ray spectrometer. Icarus 147, 498–519.

Sterling, A.C., Doschek, G.A., Feldman, U., 1993. On the absolute abundance of calcium in solar flares. Astophys. J. 404, 394–402.

Sylwester, J., Lemen, J.R., Bentley, R.D., Fludra, A., Zolcinski, M.-C., 1998. Detailed evidence for flare-to-flare variations of the coronal calcium abundance. Astophys. J. 501, 397–407.

Sylwester, J., Gaicki, I., Kordylewski, Z., Kowaliński, M., Nowak, S., Płocieniak, S., Siarkowski, M., Sylwester, B., Trzebiński, W., Bakała, J., Culhane, J.L., Whyndham, M., Bentley, R.D., Guttridge, P.R., Phillips, K.J.H., Lang, J., Brown, C.M., Doschek, G.A., Kuznetsov, V.D., Oraevsky, V.N., Stepanov, A.I., Lisin, D.V., 2005. Resik: A bent crystal X-ray spectrometer for studies of solar coronal plasma composition. Sol. Phys. 226, 45–72.

Sylwester, J., Lemen, J.R., Mewe, R., 1984. Variation in observed coronal calcium abundance of X-ray flare plasmas. Nature 310, 665–666.

Thomas, R.J., 2003. Goes_tf.pro, available at http://www.lmsal.com/solarsoft/.

Thomas, R.J., Crannell, C.J., Starr, R., 1985. Expressions to determine temperatures and emission measures for solar X-ray events from GOES measurements. Sol. Phys. 95, 323–329.

Trombka, J.I., Squyres, S.W., Brückner, J., Boynton, W.V., Reedy, R.C., McCoy, T.J., Gorenstein, P., Evans, L.G., Arnold, J.R., Starr, R.D., Nittler, L.R., Murphy, M.E., Mikheeva, I., McNutt, R.L., McClanahan, T.P., McCartney, E., Goldsten, J.O., Gold, R.E., Floyd, S.R., Clark, P.E., Burbine, T.H., Bhangoo, J.S., Bailey, S.H., Petaev, M., 2000. The elemental composition of Asteroid 433 Eros: Results of the NEAR-Shoemaker X-ray spectrometer. Science 289, 2101–2105.

Veverka, J., Robinson, M., Thomas, P., Murchie, S., Bell, J.F., Izenberg, N., Chapman, C., Harch, A., Bell, M., Carcich, B., Cheng, A., Clark, B., Domingue, D., Dunham, D., Farquhar, R., Gaffey, M.J., Hawkins, E., Joseph, J., Kirk, R., Li, H., Lucey, P., Malin, M., Martin, P., McFadden, L., Merline, W.J., Miller, J.K., Owen, W.M., Peterson, C., Prockter, L., Warren, J., Wellnitz, D., Williams, B.G., Yeomans, D.K., 2000. NEAR at Eros: Imaging and spectral results. Science 289, 2088–2097.

Watters, T.R., Prinz, M., 1979. Aubrites – Their origin and relationship to enstatite chondrites. Lunar Planet. Sci. 10, 1073–1093.

Yanai, K., Kojima, H., 1995. Catalogue of the Antarctic Meteorites. National Institute of Polar Research, Tokyo. 230 pp.

Yoshimori, M., Okudaira, K., Hirasima, Y., Igarashi, T., Akasaka, M., Takai, Y., Morimoto, K., Watanabe, T., Ohki, K., Nishimura, J., 1991. The wide band spectrometer on the Solar-A. Sol. Phys. 136, 69–88.

Zuber, M.T., Smith, D.E., Cheng, A.F., Garvin, J.B., Aharonson, O., Cole, T.D., Dunn, P.J., Guo, Y., Lemoine, F.G., Neumann, G.A., Rowlands, D.D., Torrence, M.H., 2000. The shape of 433 Eros from the NEAR-Shoemaker laser rangefinder. Science 289, 2097–2101.